

Fully coupled model for simulating highly nonlinear dynamic behaviors of a bubble near an elastic-plastic thin-walled plate

Wenbin Wu,^{1,2,3} Moubin Liu ,^{1,2,3,*} A-Man Zhang,^{4,†} and Yun-Long Liu⁴

¹College of Engineering, Peking University, Beijing 100871, China

²Institute of Ocean Research, Peking University, Beijing 100871, China

³State Key Laboratory for Turbulence and Complex systems, Peking University, Beijing 100871, China

⁴College of Shipbuilding Engineering, Harbin Engineering University, Harbin 150001, China



(Received 9 May 2020; accepted 11 December 2020; published 25 January 2021)

Existing studies of bubble-structure interaction mainly focus on the interaction between a bubble and a movable rigid body or deformable linear elastic structure. The strong nonlinear interaction of a bubble with an elastic-plastic plate has rarely been studied while the inherent dynamic behavior is not clear. In this paper, we develop a three-dimensional fully coupled model to investigate the interaction between a bubble and an elastic-plastic thin-walled plate, which can consider the fluid disturbance on both sides of the thin-walled plate. In this developed model, the dynamic behaviors of the bubble are obtained by the boundary integral method based on the potential flow theory, and the nonlinear elastic-plastic responses of the structure are resolved by the explicit finite element method on the basis of the Mindlin-Reissner plate theory. The structural nonlinear responses are incorporated into the fluid boundary integral equation (BIE), and the extra relation between the ϕ_t (time derivative of velocity potential) jump across the two sides of the thin-walled plate and its normal derivative $\phi_{,n}$ is derived, which can describe the hydrodynamic balance on both sides of the submerged plate. The derived relation is added to the BIE about ϕ_t , so that the bubble loading acting on the plate can be accurately calculated. The established coupled model is validated by comparing with experimental results. Using this numerical model, the influence of the standoff distance and plate thickness on the bubble-plate interaction is discussed. Subjected to the violent loading from the bubble, the oscillation characteristics and elastic-plastic deformation of the plate are analyzed. Due to the elastic-plastic effects of the plate, the bubble can display different interesting featured patterns, including attractive motion, repulsive motion, or splitting.

DOI: [10.1103/PhysRevFluids.6.013605](https://doi.org/10.1103/PhysRevFluids.6.013605)

I. INTRODUCTION

The bubble-structure interaction is a classical problem in fluid mechanics. It is associated with many engineering areas. In ocean engineering, the underwater explosion bubble can cause serious damage to the naval ships and submarines. In some industrial applications, cavitation bubbles lead to the surface erosion of nearby machinery, such as ship propeller blades, turbines, and hydraulic equipment [1,2]. In the medical ultrasound field, the dynamics of the microbubbles coated with a stabilizer shell in an ultrasound field play an important role in the applications of the ultrasound contrast agents and drug-carrier capsules [3–5]. In ultrasound cleaning, the cavitation bubbles around the ultrasound scaler can be effectively used to remove biofilm [6]. Although the bubble-structure

*mbliu@pku.edu.cn

†zhangaman@hrbeu.edu.cn

interaction is utilized in so many engineering applications, the fully nonlinear coupled mechanisms behind the bubble-structure interaction have not been clarified well.

During recent decades, the boundary element method (BEM) has been widely used in the bubble dynamics field, due to its powerful advantage in computational efficiency [7–10]. The dynamics of bubbles near simple boundaries (free surface or rigid fixed wall) have been extensively investigated in axisymmetric and three-dimensional (3D) cases [11–14]. By combining the BEM bubble solver with the structural solver in commercial finite element software, several researchers have simulated the dynamic interaction between the bubble and deformable structures [15–18]. They treated the variable transfer between two separate solvers, which easily results in a time difference between the physical variables in the bubble solver and structure solver [15]. In general, the loosely coupled algorithm cannot ensure the accuracy and stability of the whole fluid-structure interaction (FSI) model [19]. Accordingly, it is essential that we develop the fully coupled model to accurately investigate the nonlinear coupled interaction between bubble and structure.

For the fully coupled investigation on the bubble-structure interaction, it is required to solve all the unknowns simultaneously. The determination of the hydrodynamic load p along the structure boundary becomes the key difficulty in fully coupled schemes, while p is solved by the nonlinear Bernoulli equation,

$$p = -\rho_l(\phi_t + \frac{1}{2}\nabla\phi \cdot \nabla\phi + gz), \quad (1)$$

where ρ_l is the fluid density, ϕ is the velocity potential, ϕ_t is the Eulerian time derivative of the potential, g is the gravity acceleration, and z is the spatial position in the gravity direction. According to the acceleration potential theory [20], both ϕ_t and its normal derivative $\phi_{,n}$ are unknowns along the structure boundary, since these depend on structural motion. The fully nonlinear coupled model has to overcome the inherent challenging numerical problem to compute the bubble loading. Consequently, the investigations on the fully nonlinear interaction between the bubble and structure are relatively rare. Inspired by the wave-body interaction problems, several strategies have until recently been proposed to treat the complicated structure boundary condition and establish the fully coupled bubble-structure model. (1) Mode superposition method: Liu *et al.* [21] adopted the mode superposition method to study the interaction between the bubble and a deformable floating body, where ϕ_t is computed by the linear decomposition. Each mode component of ϕ_t can be obtained by solving the corresponding boundary integral equation (BIE). A number of BIEs must be solved at each time step, which inevitably leads to a time consuming algorithm [22], and this method cannot consider the material and geometric nonlinearity. (2) Auxiliary function method: Li *et al.* [19] employed the auxiliary function method to investigate the nonlinear interaction between the bubble and a movable rigid sphere. By introducing the artificial potential, the structural accelerations are solved directly. It is an indirect method, where ϕ_t and hydrodynamic load cannot be explicitly calculated [23]. (3) Implicit boundary method: Zhang *et al.* [24] applied the implicit boundary method to the bubble dynamics field and simulated the interaction between the bubble and elastic-plastic structure. Compared with the mode superposition and auxiliary function method, the implicit boundary method is obviously less time consuming, since only two BIEs are solved at each time step, and the hydrodynamic load is explicitly obtained [23]. It should be noted that the extension of the interaction between a bubble and a rigid body (and linear elastic structure) to that with an elastic-plastic structure is not trivial. In order to describe the nonlinear structural dynamic response, the rigid body (and linear elastic structure) kinematic model is insufficient and a self-programmed comprehensive structural nonlinear dynamic model is needed. The nonlinear geometry effects caused by the large deformation and the material model of plasticity should be considered in the FSI model.

In this study, we focus on the dynamic interaction between a bubble and a thin-walled elastic-plastic plate. The sketch of the coupled interaction is shown in Fig. 1. The Cartesian coordinate system $O\text{-}xyz$ is established at the initial bubble center, where the z axis points to the opposite direction of the gravity. The initial distance between the bubble center and the structure is d . The entire fluid field boundary S consists of the bubble surface S_b , and two sides of the thin-walled

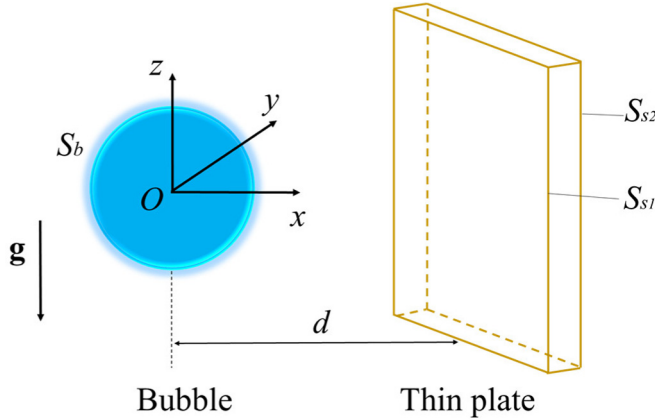


FIG. 1. Sketch of interaction between a bubble and a plate.

plate S_{s1} and S_{s2} . During the dynamic interaction process, the structural deformation is a result of the hydrodynamic loading on both sides of the structure wet surface. Therefore, the fluid load information on both sides of the thin-walled structure needs to be obtained simultaneously. However, most of the published works related to bubble-structure interaction consider the hydrodynamic load only on one side of the structure surface. It is inadequate for accurately describing the FSI phenomenon. In order to investigate the physical mechanism behind the bubble-thin-walled plate interaction, we further develop the fully coupled model which can simultaneously account for the fluid disturbance on both sides of the thin-walled plate. The interaction between a bubble and submerged thin-walled structures can be observed in numerous engineering applications. For example, in ocean engineering, the thin-walled plate is common in the body structures of ships. The interaction mechanism between the explosion bubble and the thin plate plays a key role in evaluating the survivability of naval ship structures [25]. In biomedical and clinical therapies, the work on the bubble dynamics near thin-walled tissues has motivated interesting applications such as drug delivery [5] and shock lithotripsy [26]. Therefore, it is necessary to investigate and understand the bubble dynamic behaviors near the submerged thin-walled structure.

The objective of the present work is to develop a 3D fully coupled model, where the structural motion couples with the flow field on two sides of the thin-walled plate. Then we use the model to study highly nonlinear coupled effects between a bubble and an elastic-plastic thin-walled plate. The present FSI model includes three parts, the fluid module, structure module, and coupling module. In the fluid module, the bubble violent dynamic behaviors are solved by the BEM. The mixed Eulerian-Lagrangian scheme is adopted, where the Laplace equation is resolved in the Eulerian framework while boundary values are updated in the Lagrangian manner. To eliminate the singular integral caused by the dipole on the two sides of the thin-walled plate, both sides of the plate are discretized into the same spatial mesh. In the structure module, the explicit finite element method (EFEM) is employed to describe the structural nonlinear dynamic behaviors. Based on the Mindlin-Reissner plate theory, the stress components, including the in-plane stress, bending moment, and transverse shear stress inside the elastic-plastic plate, are calculated. The center difference scheme is utilized to update the structural dynamic responses. In the coupling module, the nonlinear structural dynamic model is incorporated into the original BIEs. According to the displacement compatibility and hydrodynamic balance condition along the plate, we derive the extra link between the difference between ϕ_t on both sides of the plate and ϕ_{tn} on the plate surface. The derived implicit relation is used to determine the bubble loading acting on the plate midsurface. Using this fully nonlinear coupled model, the strong nonlinear coupled effects between the bubble and submerged plate are studied. The influence of the standoff distance and plate thickness on the bubble-structure interaction

(including the nonlinear bubble dynamic behaviors and elastic-plastic deformation mode of the plate) are discussed.

II. THREE-DIMENSIONAL FULLY COUPLED MODEL

A. Dynamics model of the bubble

On the basis of the potential flow assumption, the velocity potential ϕ and its derivative on the normal direction ϕ_n satisfy the BIE [27,28],

$$\alpha(\mathbf{r})\phi(\mathbf{r}) = \int_S \left[\phi_n(\mathbf{q})G(\mathbf{r}, \mathbf{q}) - \phi(\mathbf{q})\frac{\partial G(\mathbf{r}, \mathbf{q})}{\partial n} \right] dS, \quad (2)$$

where \mathbf{r} denotes the position vector of the controlling point on the fluid field boundary, \mathbf{q} is the position vector of the integral point, $a(\mathbf{r})$ is the solid angle at the point \mathbf{r} , and \mathbf{n} is the unit normal vector pointing to the fluid domain. The Green's function is $G(\mathbf{r}, \mathbf{q}) = 1/|\mathbf{r} - \mathbf{q}|$.

On the bubble surface S_b , the fully nonlinear kinematic condition and dynamic condition are as follows,

$$\frac{d\mathbf{r}}{dt} = \nabla\phi \quad \text{on } S_b, \quad (3)$$

$$\frac{d\phi}{dt} = \frac{P_\infty - P_v - P_b}{\rho_l} - gz + \frac{|\nabla\phi|^2}{2} \quad \text{on } S_b, \quad (4)$$

where P_b is the bubble inner pressure, and P_∞ denotes the hydrostatic pressure at the plane $z = 0$. $P_\infty = P_{atm} + \rho_l gh$, where P_{atm} denotes the atmosphere pressure. P_v is the vapor pressure. Equations (3) and (4) are integrated in the time domain to update the position and potential ϕ^b of the nodes on the bubble surface. The Dirichlet boundary condition for the BIE can be specified,

$$\phi = \phi^b. \quad (5)$$

On the structure wet surface S_s , the boundary condition can be expressed as the Neumann condition for ϕ ,

$$\phi_n = \mathbf{v} \cdot \mathbf{n} \quad \text{on } S_s, \quad (6)$$

where \mathbf{v} denotes the velocity vector of the material point on the wet surface.

The system of BIEs is closed by the equation of state. The gas flow inside the bubble satisfies the adiabatic law [29],

$$P_b = P_0 \left(\frac{V_0}{V_b} \right)^\lambda, \quad (7)$$

where V_0 and P_0 are the initial volume and inner pressure of the bubble, respectively. V_b is the transient bubble volume. λ is the specific heat ratio.

The BIE (2) can be written in the following matrix form [13],

$$\begin{bmatrix} \mathbf{G}_{bb} & -\mathbf{H}_{bs} \\ \mathbf{G}_{sb} & -\mathbf{H}_{ss} \end{bmatrix} \begin{bmatrix} \Phi_{n,b} \\ \Phi_s \end{bmatrix} = \begin{bmatrix} \mathbf{H}_{bb} & -\mathbf{G}_{bs} \\ \mathbf{H}_{sb} & -\mathbf{G}_{ss} \end{bmatrix} \begin{bmatrix} \Phi_b \\ \Phi_{n,s} \end{bmatrix}, \quad (8)$$

where \mathbf{G} and \mathbf{H} are the coefficient matrices. \mathbf{G} involves the influence of the first term in the right-hand side (RHS) of the BIE (2), and \mathbf{H} involves the influence of the solid angle and second term in the RHS of the BIE (2). The subscripts b and s represent the physical variable on the bubble and structure surface, respectively. The RHSs of Eq. (8) are knowns, including the velocity potential on S_b (Φ_b) and the normal velocity on S_s ($\Phi_{n,s}$). For the boundary value problem Eq. (2), $\Phi_{n,b}$ and Φ_s can be solved directly.

In the present study, the fluid boundaries are discretized into the linear triangular elements. For the fully submerged thin-walled plate, the plate surface on two sides, S_{s1} and S_{s2} , should both

be considered in the BIE (8). The thin plate's thickness is much smaller than the lateral spans. Therefore, the discretized dipole easily causes high order singular integrals at the source point when we deal with the BIE (8). In order to eliminate the above singular integrals, the plate surface S_{s1} and S_{s2} are discretized into the same triangular mesh. The point at the same location on two sides of the plate satisfies

$$\phi_n|_{S_{s2}} = -\phi_n|_{S_{s1}}. \quad (9)$$

After the BIE (2) is solved at any given time t , the geometric shape and velocity potential on S_b must be updated to the next time step. The Euler forward method and the mixed Eulerian-Lagrangian scheme [30] are adopted,

$$\mathbf{r}(t + \Delta t_b) = \mathbf{r}(t) + \Delta t_b \frac{d\mathbf{r}}{dt}(t), \quad (10)$$

$$\phi(t + \Delta t_b) = \phi(t) + \Delta t_b \frac{d\phi}{dt}(t), \quad (11)$$

where Δt_b is the time step in the fluid module. To guarantee the stability of the bubble dynamics model, the determination of Δt_b is chosen as [31]

$$\Delta t_b = R_m \sqrt{\frac{P_\infty}{\rho_l} \frac{\delta\phi}{\max\left(\left|\frac{P_\infty - P_b}{\rho_l} - \frac{1}{2}|\nabla\phi|^2 - gz\right|\right)}}, \quad (12)$$

where the maximum in the denominator of (12) is taken over all the nodes on the bubble and plate surface. This condition can ensure that the velocity potential on the bubble surface changes within $\delta\phi R_m \sqrt{P_\infty/\rho_l}$ during each time step. The parameter $\delta\phi = 0.008$ in this paper. R_m is the maximum bubble radius.

B. Dynamics model of the structure

The oscillation period of a bubble with high pressure is usually very short [15,24]. Therefore, in the present study, the structural responses are solved by the explicit finite element method (EFEM), which is an efficient tool to deal with the nonlinear transient structural responses. The structural code is developed in house, which can output the structural variables and easily fulfill the fully coupled interaction between bubble and structure. The governing equation of structural dynamics in the EFEM can be written in the nodal discretized form [32],

$$m\mathbf{a} = \mathbf{F}^{\text{ext}} - \mathbf{F}^{\text{int}}, \quad (13)$$

where m is the nodal lumped mass, \mathbf{a} is the nodal acceleration vector, the external force \mathbf{F}^{ext} is the bubble loading acting on the plate, and \mathbf{F}^{int} is the nodal internal force vector due to the elastic-plastic stress of the plate. The computation of \mathbf{F}^{ext} is discussed in detail in Sec. II C. The solution of \mathbf{F}^{int} is described in the following part of this section.

The central difference scheme is employed to explicitly update the velocity \mathbf{v} and displacement \mathbf{u} from the n th moment to the $(n+1)$ th moment [33,34],

$$\mathbf{v}^{n+1/2} = \mathbf{v}^{n-1/2} + \mathbf{a}^n \Delta t_s^{n+1/2}, \quad (14)$$

$$\mathbf{u}^{n+1} = \mathbf{u}^n + \mathbf{v}^{n+1/2} \Delta t_s^{n+1}, \quad (15)$$

where $\Delta t_s^{n+1/2} = \frac{1}{2}(\Delta t_s^n + \Delta t_s^{n+1})$. The time step in the structure module Δt_s is defined as [35,36]

$$\Delta t_s = \frac{l_e}{c}, \quad (16)$$

where $l_e = 2A/L$. A is the element area and L is the longest edge length of the element. The wave speed $c = \sqrt{E/\rho_S(1-\nu^2)}$, where E is the elastic modulus, ρ_S is the material density, and ν is the Poisson ratio of the structure [32].

In the structure module, the midsurface of the thin-walled plate is discretized into the three-node triangular element. In order to conveniently transfer the variables between the fluid and structure solver, the midsurface is discretized with the same spatial mesh in the fluid module. The Reissner-Mindlin plate theory is adopted to model the structural dynamics in this paper. The local corotational coordinate system $\hat{x}\hat{y}\hat{z}$ is established, whose unit vectors are $\hat{\mathbf{e}}_1$, $\hat{\mathbf{e}}_2$, and $\hat{\mathbf{e}}_3$. $\hat{\mathbf{e}}_1$ and $\hat{\mathbf{e}}_2$ remain tangent to the shell midsurface, and $\hat{\mathbf{e}}_3 = \hat{\mathbf{e}}_1 \times \hat{\mathbf{e}}_2$ is normal to the midsurface [37]. The transform matrix \mathbf{T} between the global and local corotational coordinate system is

$$[\mathbf{T}] = [\hat{\mathbf{e}}_1 \quad \hat{\mathbf{e}}_2 \quad \hat{\mathbf{e}}_3]^T. \quad (17)$$

Hereafter, the variables in the local system will be denoted by a hat \wedge . According to the Reissner-Mindlin kinematic hypothesis, the velocity in the plate $\hat{\mathbf{v}}$ has the following form [32],

$$\hat{\mathbf{v}} = \hat{\mathbf{v}}^m - \hat{z}\hat{\mathbf{e}}_3 \times \hat{\boldsymbol{\omega}} = \begin{bmatrix} \hat{v}_x^m + \hat{z}\hat{\omega}_y \\ \hat{v}_y^m - \hat{z}\hat{\omega}_x \\ \hat{v}_z^m \end{bmatrix}, \quad (18)$$

where $\hat{\mathbf{v}}^m$ represents the translation velocity at midsurface and $\hat{\boldsymbol{\omega}}$ represents the rotation angular velocity. \hat{z} is the distance from the midsurface in the thickness direction $\hat{\mathbf{e}}_3$.

The velocity-strain rate relationship is [37]

$$\hat{\mathbf{d}} = \frac{1}{2}(\hat{\mathbf{L}} + \hat{\mathbf{L}}^T), \quad \hat{d}_{ij} = \frac{1}{2}(\hat{L}_{ij} + \hat{L}_{ji}) = \frac{1}{2} \left(\frac{\partial \hat{v}_i}{\partial \hat{x}_j} + \frac{\partial \hat{v}_j}{\partial \hat{x}_i} \right), \quad (19)$$

where $\hat{\mathbf{d}}$ denotes the strain rate tensor. $\hat{\mathbf{L}}$ is the velocity gradient in the local coordinate system. The subscripts i, j represent the local axis, and $i, j = \hat{x}, \hat{y}, \hat{z}$.

With the nodal velocity values and shape functions, the velocity vector can be expressed as [32]

$$\hat{\mathbf{v}}^m = \sum_{k=1}^3 \hat{\mathbf{v}}_k^m \varphi_k, \quad \hat{\boldsymbol{\omega}} = \sum_{k=1}^3 \hat{\boldsymbol{\omega}}_k \varphi_k, \quad (20)$$

where the subscript k denotes the nodal index in triangular shell element $k = 1, 2, 3$. φ_k is the shape function at the k th node.

Substituting the interpolated velocity field Eq. (20) into the velocity-strain rate relationship Eq. (19), we can obtain the strain rate components [38],

$$\begin{Bmatrix} \hat{d}_x \\ \hat{d}_y \\ 2\hat{d}_{xy} \end{Bmatrix} = \mathbf{B}_M \hat{\mathbf{v}}^m - \hat{z} \mathbf{B}_M \hat{\boldsymbol{\omega}}^{\text{def}}, \quad \begin{Bmatrix} 2\hat{d}_{xz} \\ 2\hat{d}_{yz} \end{Bmatrix} = \mathbf{B}_S \hat{\boldsymbol{\omega}}^{\text{def}}, \quad (21)$$

where the matrices \mathbf{B}_M and \mathbf{B}_S denote the derivatives of the nodal interpolation functions, and the detailed expressions of \mathbf{B}_M and \mathbf{B}_S can be seen from [38]. $\hat{\boldsymbol{\omega}}^{\text{def}}$ denotes the deformation rotation angular velocity, excluding effects of the rigid body rotation. The strain rate $\hat{\mathbf{d}}$ is affected by two parts, i.e., membrane stretching effects caused by the midsurface velocity $\hat{\mathbf{v}}^m$ and bending contributions caused by the angular velocity $\hat{\boldsymbol{\omega}}$ [38].

The element strain $\hat{\boldsymbol{\epsilon}}$ can be obtained by updating the strain rate \hat{d}_{ij} in the time domain, and then the corresponding element stress components $\hat{\mathbf{s}}$ can be determined by means of the constitutive model. The elastic-plastic stress tensor on the shell surface $\hat{\mathbf{s}}$ can be expressed as

$$\hat{\mathbf{s}} = \hat{\boldsymbol{\sigma}} + \hat{\boldsymbol{\tau}}. \quad (22)$$

The stress tensor includes two parts of the effects, the membrane stretching due to the in-plane elastic stress $\hat{\boldsymbol{\sigma}} = [\hat{\sigma}_x \hat{\sigma}_y]^T$ and bending moments and shear resultant caused by the shear stress

$\hat{\boldsymbol{\tau}} = [\hat{\tau}_{xy} \hat{\tau}_{xz} \hat{\tau}_{yz}]^T$ [37]. The in-plane tension $\hat{\boldsymbol{\sigma}}$ is caused by the membrane stretching. According to Hooke's law, the in-plane elastic stress $\hat{\boldsymbol{\sigma}}$ linearly depends on the strain,

$$\hat{\sigma}_x = \frac{E}{(1-\nu^2)}(\hat{\epsilon}_x + \nu\hat{\epsilon}_y), \quad \hat{\sigma}_y = \frac{E}{(1-\nu^2)}(\hat{\epsilon}_y + \nu\hat{\epsilon}_x). \quad (23)$$

The shear stress can be determined by

$$\begin{bmatrix} \hat{\tau}_{xy} \\ \hat{\tau}_{xz} \\ \hat{\tau}_{yz} \end{bmatrix} = \begin{bmatrix} E/2(1+\nu) & 0 & 0 \\ 0 & 5E/12(1+\nu) & 0 \\ 0 & 0 & 5E/12(1+\nu) \end{bmatrix} \begin{bmatrix} \hat{\epsilon}_{xy} \\ \hat{\epsilon}_{xz} \\ \hat{\epsilon}_{yz} \end{bmatrix}. \quad (24)$$

When $\hat{\mathbf{s}}$ reaches the yield stress, the von Mises rule is adopted to deal with the yield and plastic behaviors of the material. For the material model of plasticity, readers can refer to [37] for details. In this study, the bilinear constitutive model is employed to simulate the structural elastic-plastic responses.

By integrating the in-plane tension and shear stress through the shell thickness, the local resultant forces and moments can be determined,

$$\begin{aligned} \hat{f}_{xx}^R &= \int \hat{\sigma}_x d\hat{z}, & \hat{f}_{yy}^R &= \int \hat{\sigma}_y d\hat{z}, \\ \hat{f}_{xy}^R &= \int \hat{\tau}_{xy} d\hat{z}, & \hat{f}_{xz}^R &= \int \hat{\tau}_{xz} d\hat{z}, & \hat{f}_{yz}^R &= \int \hat{\tau}_{yz} d\hat{z}, \\ \hat{m}_{xx}^R &= - \int \hat{z} \hat{\sigma}_x d\hat{z}, & \hat{m}_{yy}^R &= - \int \hat{z} \hat{\sigma}_y d\hat{z}, & \hat{m}_{xy}^R &= - \int \hat{z} \hat{\tau}_{xy} d\hat{z}, \end{aligned} \quad (25)$$

where the superscript R denotes the resultant force or moment. Using the principle of virtual power and the one-point quadrature rule, the expressions of the nodal internal forces and moments in the local coordinates are obtained [38],

$$\begin{bmatrix} \hat{f}_{x1}^e \\ \hat{f}_{y1}^e \\ \hat{f}_{x2}^e \\ \hat{f}_{y2}^e \\ \hat{f}_{x3}^e \\ \hat{f}_{y3}^e \end{bmatrix} = \mathbf{AB}_M^T \begin{bmatrix} \hat{f}_{xx}^R \\ \hat{f}_{yy}^R \\ \hat{f}_{xy}^R \end{bmatrix}, \quad \begin{bmatrix} \hat{m}_{x1}^e \\ \hat{m}_{y1}^e \\ \hat{m}_{x2}^e \\ \hat{m}_{y2}^e \\ \hat{m}_{x3}^e \\ \hat{m}_{y3}^e \end{bmatrix} = \mathbf{AB}_M^T \begin{bmatrix} \hat{m}_{xx}^R \\ \hat{m}_{yy}^R \\ \hat{m}_{xy}^R \end{bmatrix} + \mathbf{AB}_S^T \begin{bmatrix} \hat{f}_{xz}^R \\ \hat{f}_{yz}^R \end{bmatrix}. \quad (26)$$

With the transform matrix \mathbf{T} , the internal force and moment in the global system O -xyz can be calculated,

$$\begin{bmatrix} F_{xk}^{\text{int}} \\ F_{yk}^{\text{int}} \\ F_{zk}^{\text{int}} \end{bmatrix} = [\mathbf{T}] \begin{bmatrix} \hat{f}_{xk}^e \\ \hat{f}_{yk}^e \\ \hat{f}_{zk}^e \end{bmatrix}, \quad \begin{bmatrix} m_{xk}^{\text{int}} \\ m_{yk}^{\text{int}} \\ m_{zk}^{\text{int}} \end{bmatrix} = [\mathbf{T}] \begin{bmatrix} \hat{m}_{xk}^e \\ \hat{m}_{yk}^e \\ 0 \end{bmatrix}. \quad (27)$$

C. Fully coupled model between the bubble and structure solvers

The resultant external force acting on the thin-walled plate depends on the difference between the hydrodynamic pressure on two sides of the plate. By integrating unsteady Bernoulli pressure along the wet surface, the resultant external force can be expressed as [24]

$$F_i^{\text{ext}} = F_i^{\text{ext}}|_{S_{S1}} - F_i^{\text{ext}}|_{S_{S2}} = \int_{S_{S1}} -\rho_l \left(\phi_t + \frac{1}{2} |\nabla \phi|^2 \right) \cdot n_i dS + \int_{S_{S2}} \rho_l \left(\phi_t + \frac{1}{2} |\nabla \phi|^2 \right) \cdot n_i dS, \quad (28)$$

where the subscript i represents the component of the variable in the i th direction ($i = x, y, z$).

On the entire fluid field boundary, ϕ_t satisfies the BIE,

$$\alpha(\mathbf{r})\phi_t(\mathbf{r}) = \int_S \left[\frac{\partial \phi_t}{\partial n}(\mathbf{q})G(\mathbf{r}, \mathbf{q}) - \phi_t(\mathbf{q})\frac{\partial G(\mathbf{r}, \mathbf{q})}{\partial n} \right] dS. \quad (29)$$

The boundary conditions on S_b and S_s are as follows [24],

$$\phi_t = \frac{P_\infty - P_v - P_b}{\rho} - gz - \frac{|\nabla \phi|^2}{2} \quad \text{on } S_b, \quad \phi_{tn} = \mathbf{a} \cdot \mathbf{n} + v(\mathbf{r}) \quad \text{on } S_s, \quad (30)$$

where $v(\mathbf{r})$ denotes the function of the local velocity on S_s . Since the motions of the fluid nodes on two sides of the thin-walled plate are opposite and equal, the relation about ϕ_{tn} between the wet surface S_{s1} and S_{s2} is

$$\phi_{tn}|_{S_{s2}} = -\phi_{tn}|_{S_{s1}}. \quad (31)$$

From Eq. (30), it can be seen that the calculation of ϕ_t depends on the structural dynamic response. However, meanwhile, ϕ_t has a direct influence on the structural deformation according to Eqs. (13) and (28). The precise computation of ϕ_t becomes a key factor for calculating the hydrodynamic force. In order to simulate the fully nonlinear interaction accurately, the governing equations of bubble and structural dynamics should be solved simultaneously. In other words, for the whole bubble-structure interaction model, the physical variables in the fluid module and structure module must be at the same time. The main challenge for the computation of ϕ_t is that both ϕ_t and ϕ_{tn} are unknowns on the structure surface. In the present study, we derive the implicit boundary condition and develop a fully coupled model to simulate the nonlinear interaction between the violent bubble and elastic-plastic thin-walled plate.

The main idea of the present method is to establish an additional relationship between ϕ_t and ϕ_{tn} on two sides of a thin-walled plate S_s . Substituting the expression of the structural acceleration given by Eq. (13) into Eq. (30) yields

$$\phi_{tn}(\mathbf{r}) = \frac{1}{m} \left(\int_{S_{s1}} p_\xi \mathbf{n}_\xi dS_\xi - \int_{S_{s2}} p_\xi \mathbf{n}_\xi dS_\xi - \mathbf{F}^{\text{int}} \right) \cdot \mathbf{n} + v(\mathbf{r}) \quad \text{on } S_s, \quad (32)$$

where p_ξ and \mathbf{n}_ξ represent the pressure and normal vector at the Gaussian integration point ξ on S_s .

Replacing the hydrodynamic pressure with the nonlinear Bernoulli equation, the implicit boundary condition which links ϕ_t and ϕ_{tn} on S_s can be obtained,

$$\phi_{tn}(\mathbf{r}) + \int_{S_{s1}} K(\mathbf{r}, \xi)\phi_t(\xi)dS_\xi - \int_{S_{s2}} K(\mathbf{r}, \xi)\phi_t(\xi)dS_\xi = \chi(\mathbf{r}) \quad \text{on } S_s, \quad (33)$$

where the kernel function $K(\mathbf{r}, \xi)$ depends on the geometry shape and structural lumped mass,

$$K(\mathbf{r}, \xi) = \frac{\rho_l}{m} \mathbf{n}(\mathbf{r}) \cdot \mathbf{n}(\xi),$$

and

$$\chi(\mathbf{r}) = - \int_{S_{s1}} \frac{1}{2} \nabla \phi_\xi \cdot \nabla \phi_\xi K(\mathbf{r}, \xi) dS + \int_{S_{s2}} \frac{1}{2} \nabla \phi_\xi \cdot \nabla \phi_\xi K(\mathbf{r}, \xi) dS - \frac{\mathbf{F}^{\text{int}} \cdot \mathbf{n}}{m} + v(\mathbf{r}).$$

The structural elastic-plastic effects are considered in the term $\chi(\mathbf{r})$. On the basis of the structural transient dynamic theory and acceleration potential method [20], we obtain the additional boundary integral equation (33) called the *implicit boundary condition*. The derived implicit condition, which

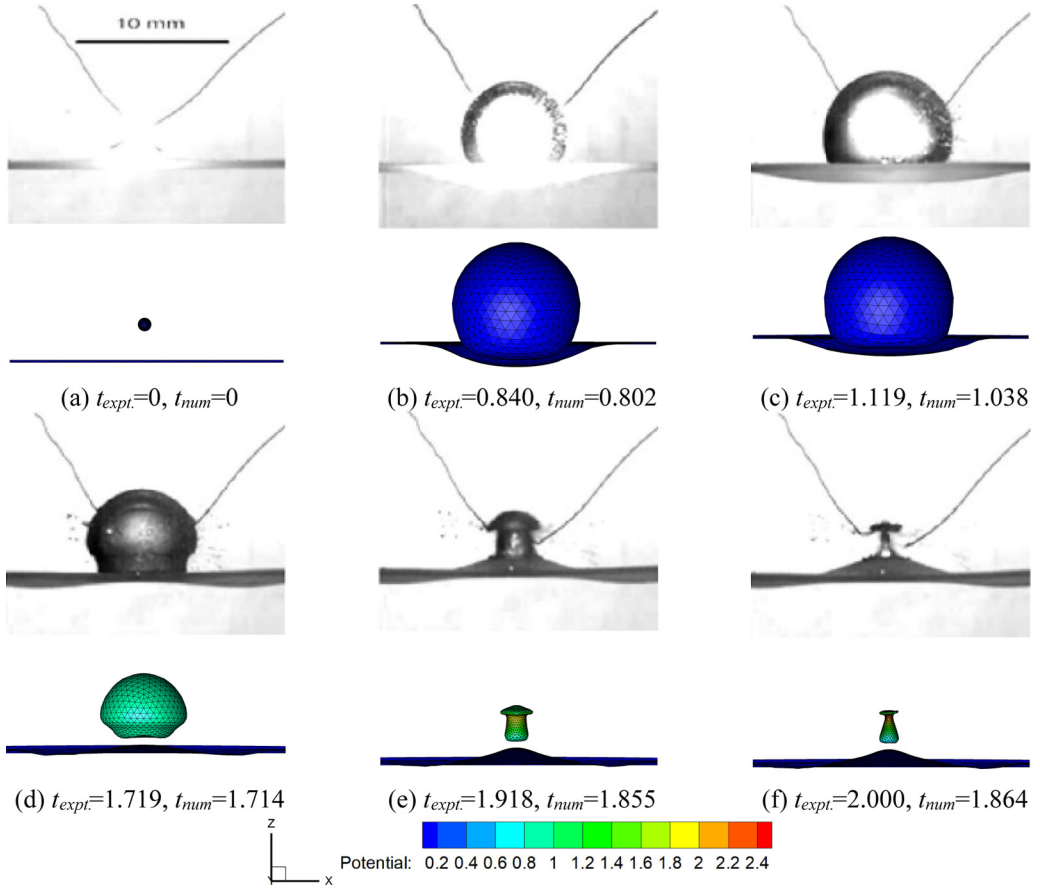


FIG. 2. Comparison of the bubble–thin membrane interaction between the experimental images [40] and numerical results at typical dimensionless moments. The parameters in the simulation are $R_m = 4.1$ mm, $R_0 = 0.419$ mm, $P_\infty = 7.844 \times 10^4$ Pa, $P_v = 0.23 \times 10^5$ Pa, $\rho_s = 1250$ kg/m³, $E = 3.16$ MPa, $\nu = 0.5$, $h = 0.299$ mm, $\gamma_w = 0.55$, $\varepsilon = 400$, and $\lambda = 1.4$.

establishes an extra relationship between ϕ_t jump across the two sides of the thin-walled plate and ϕ_{tn} , and then it is added to the original system of the BIE (29), which can be written in the matrix form,

$$\begin{bmatrix} \mathbf{G}_{bb} & -\mathbf{H}_{bs1} & -\mathbf{H}_{bs2} & \mathbf{G}_{bs1} & \mathbf{G}_{bs2} \\ \mathbf{G}_{s1b} & -\mathbf{H}_{s1s1} & -\mathbf{H}_{s1s2} & \mathbf{G}_{s1s1} & \mathbf{G}_{s1s2} \\ \mathbf{G}_{s2b} & -\mathbf{H}_{s2s1} & -\mathbf{H}_{s2s2} & \mathbf{G}_{s2s1} & \mathbf{G}_{s2s2} \\ \mathbf{0} & \mathbf{K}_{s1} & -\mathbf{K}_{s2} & \mathbf{I} & \mathbf{0} \\ \mathbf{0} & \mathbf{0} & \mathbf{0} & -\mathbf{I} & \mathbf{I} \end{bmatrix} \begin{bmatrix} \Phi_{tn,b} \\ \Phi_{t,s1} \\ \Phi_{t,s2} \\ \Phi_{tn,s1} \\ \Phi_{tn,s2} \end{bmatrix} = \begin{bmatrix} \mathbf{H}_{bb} \Phi_{t,b} \\ \mathbf{H}_{s1b} \Phi_{t,b} \\ \mathbf{H}_{s2b} \Phi_{t,b} \\ \chi \\ \mathbf{0} \end{bmatrix}, \quad (34)$$

where \mathbf{I} is a unit matrix of size $N_{s1} \times N_{s1}$. N_{s1} is the number of nodes on the single side of the thin-walled plate. The subscripts $s1$ and $s2$ denote the nodes on the wet surface S_{s1} and S_{s2} , respectively. The RHS of Eq. (34) contains known variables. The column vectors in the left-hand side of Eq. (34) are unknown variables, which must be solved. The new system of BIE (34) includes $(N + 2N_{s1})$ linear discretized algebraic equations with $(N + 2N_{s1})$ unknowns, where N is the total number of nodes on the fluid boundary S . This means the existence and uniqueness of a solution. Therefore, ϕ_t on S_s can be calculated directly and accurately. With the known ϕ_t , the external resultant force can

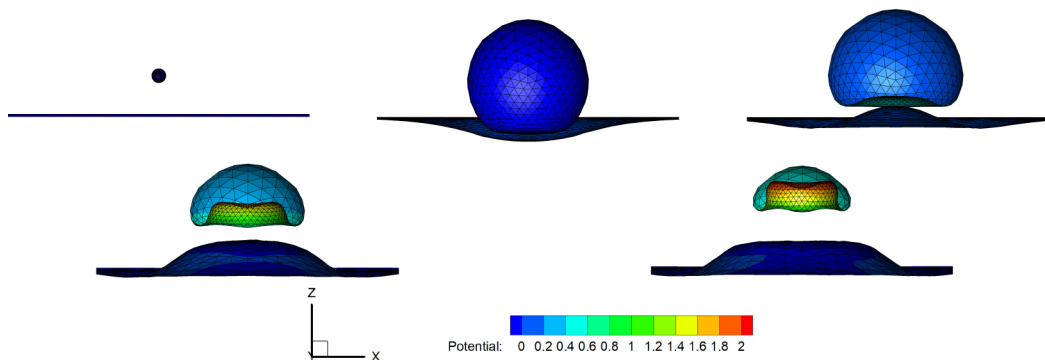


FIG. 3. Dimensionless velocity potential contour of bubble–thin membrane interaction results using Eq. (36) at the nondimensional times $t = 0, 0.384, 0.837, 1.144,$ and 1.262 . All the parameters are the same as in Fig. 2.

be calculated using Eq. (28), and then it is transferred to the structure module. Through Eq. (13), the structural nodal acceleration can be obtained. Then the structural nodal displacement and velocity are explicitly integrated to the next time step. It should be noted that the structure undergoes dynamic responses under the combined action of the bubble hydrodynamic loading and additional mass force. Consequently, in the present fully coupled model, the effects of the additional mass force have been considered in the term $\Phi_{t,s}$.

In the present study, thanks to the derived implicit boundary method, the whole fully coupled bubble–structure interaction model can be successfully decoupled into fluid module and structure module. The fluid module and structure module adopt their respective time steps Δt_b and Δt_s to update their own information. The choice of the time step Δt for the whole bubble–structure interaction model follows the criterion in [24], $\Delta t = \min(500\Delta t_s, \Delta t_b)$. Within each time step Δt , the fluid solver is executed at first, where nonlinear bubble dynamic behaviors are simulated. By solving Eqs. (34) and (28), the external force can be computed, and then it is transferred to the structure module. In the structure solver, with the input external force, the transient nonlinear dynamic responses of the plate can be solved. The external force is assumed to be a constant during Δt . When $t_s + \Delta t_s > t + \Delta t_b$, we modify Δt_s as $\Delta t_s^{\text{modified}} = t + \Delta t_b - t_s$, so that the time discrepancy between the fluid and structure module can be eliminated. Then we output the structural information (including the nodal displacement, velocity, mass, and internal force) to the fluid module. The present bubble–structure interaction model can guarantee that all the physical information in Eq. (34) is at the same time.

III. NUMERICAL RESULTS AND DISCUSSIONS

In this study, we describe the bubble dynamic behaviors in the nondimensionalization form. The maximal bubble radius R_m , fluid density ρ_l , and $(P_\infty - P_v)$ are chosen as the reference length L_{ref} , reference density ρ_{ref} , and reference pressure P_{ref} respectively. Therefore, the reference velocity $V_{\text{ref}} = \sqrt{P_{\text{ref}}/\rho_{\text{ref}}}$, the reference time $T_{\text{ref}} = L_{\text{ref}}\sqrt{\rho_{\text{ref}}/P_{\text{ref}}}$, and the reference velocity potential $\phi_{\text{ref}} = L_{\text{ref}}\sqrt{P_{\text{ref}}/\rho_{\text{ref}}}$, and the nondimensional parameters are introduced. The distance parameter $\gamma_w = d/R_m$, which denotes the dimensionless distance of the bubble from the plate [2]. The strength parameter $\varepsilon = P_0/P_{\text{ref}}$, which is the ratio of the initial bubble pressure and ambient pressure [15]. The initial dimensionless bubble radius can be directly determined by the strength parameter [15,39]. In this paper, the fluid density $\rho_l = 1000 \text{ kg/m}^3$, atmosphere pressure $P_{\text{atm}} = 1.0 \times 10^5 \text{ Pa}$, and gravity acceleration $g = 9.8 \text{ m/s}^2$. Hereafter, use of the variables without indicating their units indicates the nondimensional variables.

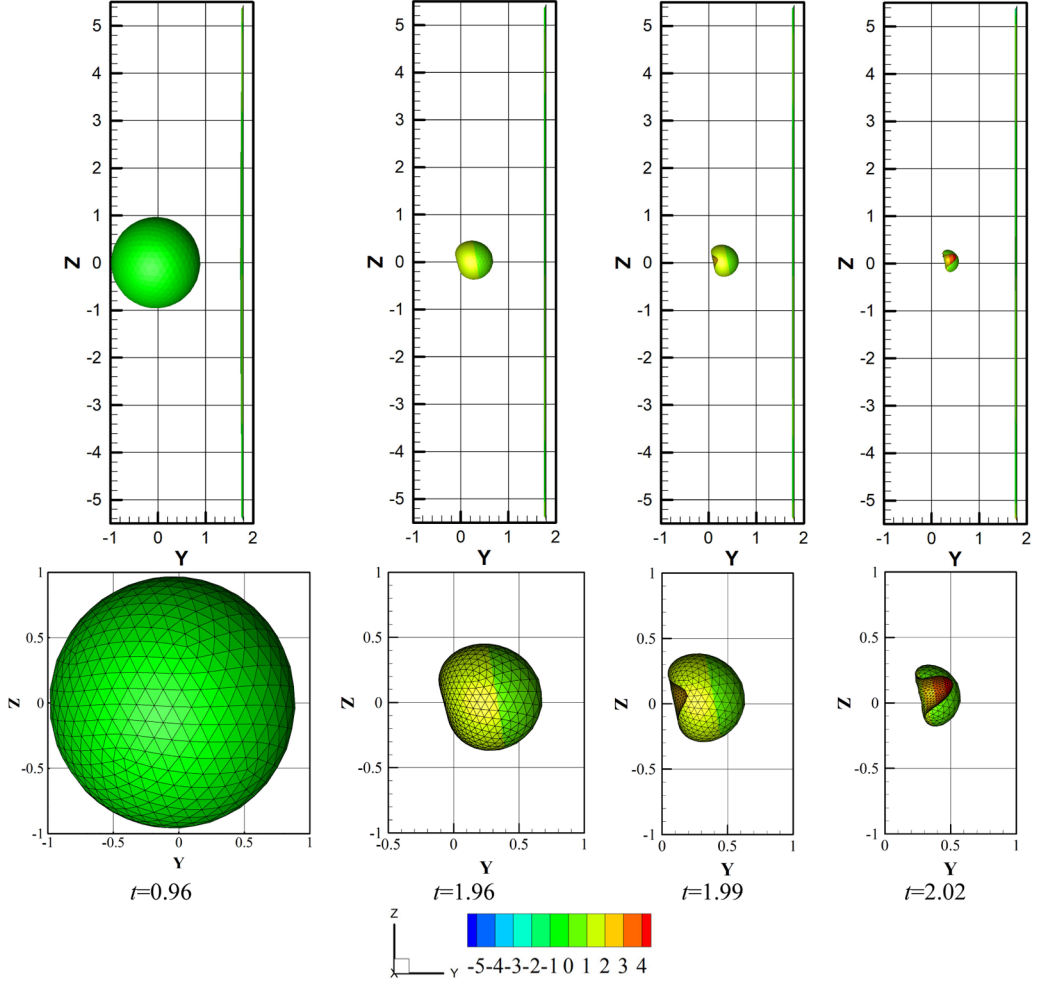


FIG. 4. Dimensionless velocity potential contour of bubble dynamics near a thin-walled plate with $\gamma_w = 1.75$ at typical nondimensional times. The other parameters are $R_m = 0.112$ m, $R_0 = 8.904$ mm, $P_\infty = 1.098 \times 10^5$ Pa, $P_v = 0$, $\rho_s = 7850$ kg/m³, $E = 203$ GPa, $\nu = 0.3$, $\sigma_0 = 235$ MPa, $E_T = 400$ MPa, $h = 20$ mm, $\varepsilon = 588.76$, and $\lambda = 1.25$. Top: The interaction between the bubble and a thin-walled plate. Below: An enlarged view of the evolution of the bubble.

A. Validation of the numerical model

To validate the accuracy of the present fully coupled model, we compare the numerical results with the experimental results in [40]. The bubble experiment is conducted in a $10 \times 15 \times 15$ cm³ water tank. The bubble is generated by the discharge of the electrical spark. The membrane is located at the center of the water tank, and the spark-generated bubble is located above it. A silicon rubber sheet is used as an elastic thin membrane. The initial length L_x , width L_y , and thickness of the unstretched membrane are 47, 30, and 0.35 mm, respectively. The membrane is stretched in the x direction under the action of the force $F = 5.65$ N so that the membrane length L_x is up to 55 mm. The material properties of the stretched membrane are as follows: Young's modulus $E = 3.16$ MPa, density $\rho_s = 1250$ kg m⁻³, and Poisson's ratio is 0.5. The maximum bubble radius is 4.1 mm. The dimensionless distance parameter $\gamma_w = 0.55$. In the numerical simulation, we set

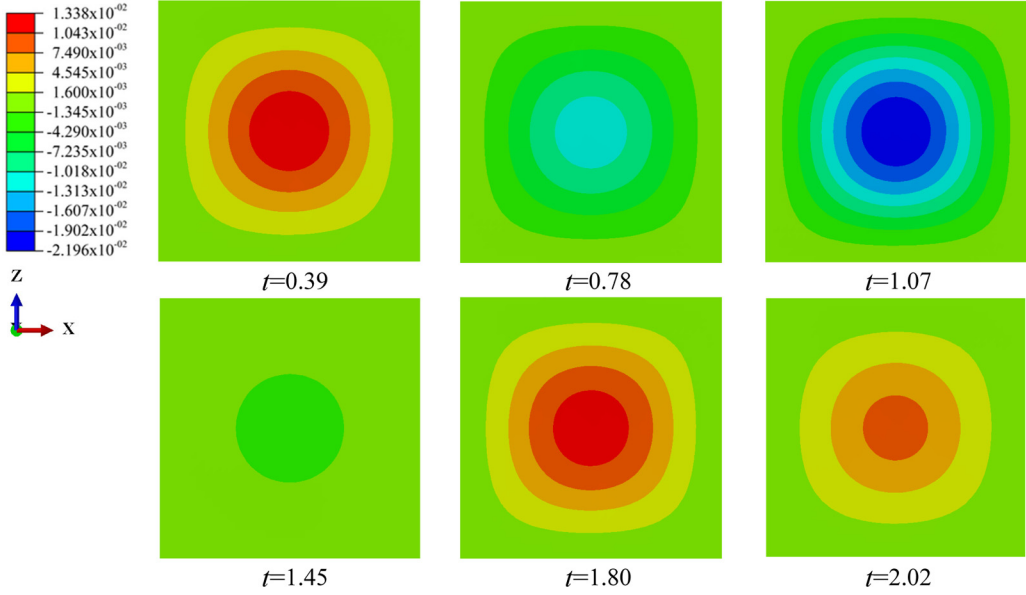


FIG. 5. Dimensionless displacement contour of plate in the y direction at $\gamma_w = 1.75$. All the parameters are the same as in Fig. 4.

the strength parameter $\varepsilon = 400$, and its corresponding initial bubble radius $R_0/R_m = 0.102$ [15]. The ratio of the specific heat $\lambda = 1.4$. The membrane boundary is rigidly fixed. Buogo and Cannelli [41] found that the vapor pressure was extremely high ($P_v = 0.3 \times 10^5$ Pa) in the spark-generated bubble experiment. The phenomenon might be attributed to the heating of the bubble surface when the bubble is generated by the electric discharge [42]. To accommodate this phenomenon, the vapor pressure is taken to be $P_v = 0.23 \times 10^5$ Pa in this section.

For the thin membrane element, the rotational degrees of freedom at the nodes are constrained, and the translational degrees of freedom cause the membrane strain [38]. Therefore, to simulate the stretched membrane deformation in this section, we set $\hat{\omega}_{xk}^{\text{def}} = \hat{\omega}_{yk}^{\text{def}} = \hat{v}_{zk} = 0$ in Eq. (21), and the stretched effects of the membrane can be considered by enforcing a surface tension $\chi = F/L_y =$

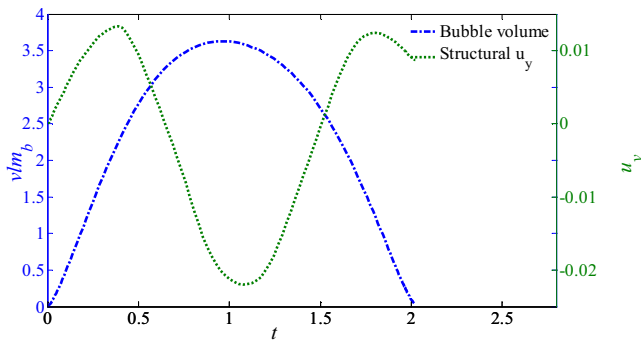


FIG. 6. Time history of the dimensionless bubble volume and plate center displacement for the case shown in Fig. 4.

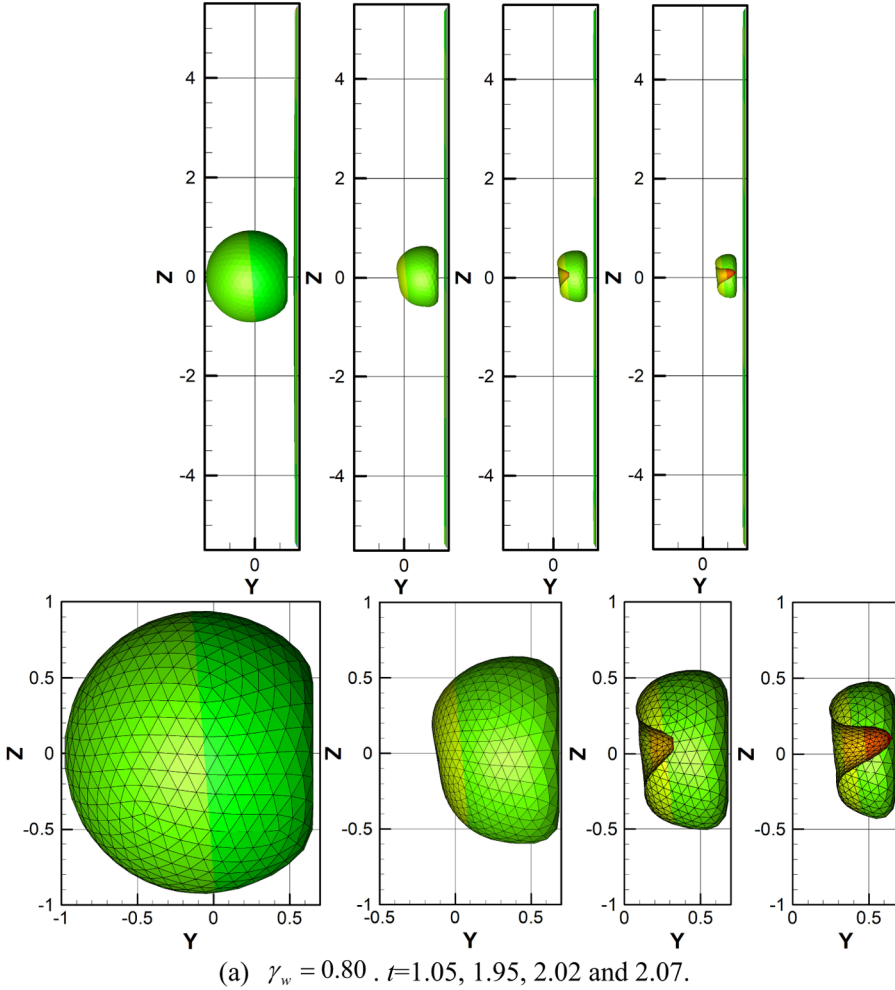


FIG. 7. Dimensionless velocity potential contour of bubble dynamics near a submerged plate for various distance parameters $\gamma_w = 0.80, 1.00, 1.25,$ and 1.50 with the remaining parameters being the same as in Fig. 4. Top: The interaction between the bubble and a thin-walled plate. Below: An enlarged view of the evolution of the bubble.

188.3 N/m [42,43]. The resultant force including the stretched effects can be expressed as

$$F_i^{\text{ext}} = \int_{S_{S1}} -\rho_l \left(\phi_t + \frac{1}{2} |\nabla \phi|^2 - \chi \kappa \right) \cdot n_i dS + \int_{S_{S2}} \rho_l \left(\phi_t + \frac{1}{2} |\nabla \phi|^2 \right) \cdot n_i dS, \quad (35)$$

where κ denotes the curvature in the stretched direction (x direction).

The comparison between the experimental images and numerical results is displayed in Fig. 2. The bubble is generated at $t = 0$. During the expansion phase, the bubble remains nearly spherical, and the thin membrane moves downward to form a dip [panel (b)]. The bubble expands to reach its maximum radius in panel (c). Then the bubble begins to collapse. The upper surface of the bubble undergoes nearly spherical collapse, and the lower surface is flattened by the nearby boundary. During the collapse phase, a mushroom shaped bubble forms and the thin membrane is attracted upward in frames (d), (e). Eventually, the bubble splits in frame (f). Both the structure deformation and bubble shapes correspond well with the experimental results, which indicates the effectiveness

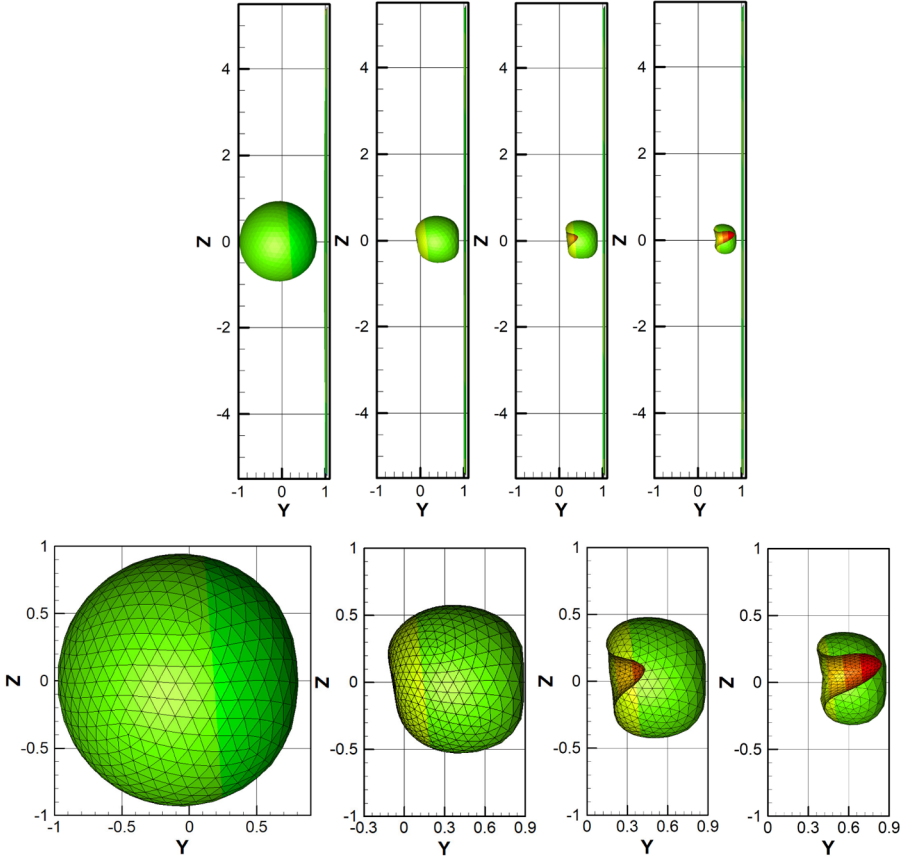

 (b) $\gamma_w = 1.00$, $t=1.05, 1.96, 2.03$ and 2.09 .

FIG. 7. (Continued.).

of the present model in simulating the interaction between the bubble and the thin-walled structure. Because it is hard to match exactly the initiation of the electric spark-generated bubble in the numerical simulation, there is a certain difference in timing between the experimental results and numerical results [42,43].

Most of the previous coupled models [10,18,19] consider the hydrodynamic loading only on the single side of the plate S_{S1} . It assumes that the hydrodynamic loading on the other side of the plate S_{S2} is the hydrostatic pressure all the time. Therefore, in the previous coupled models, the resultant force acting on the structure surface is

$$F_i^{\text{ext}} = \int_{S_{S1}} -\rho_l \left(\phi_t + \frac{1}{2} |\nabla \phi|^2 - \chi \kappa \right) \cdot n_i dS, \quad (36)$$

By substituting Eq. (36) for Eq. (35), the coupled model is adopted to simulate the above electric spark-generated bubble experiment with the same parameters. The numerical results obtained by using Eq. (36) are shown in Fig. 3. At the end of the collapse phase, the bubble forms an upward jet. For this case, the bubble shapes and structural deformation in Fig. 3 are totally different from the experimental results [40] in Fig. 2. Compared with the results in Fig. 3, the numerical results obtained by the present model show better agreement with the experimental images. This demonstrates the advantages of the present model in handling the bubble–thin plate interaction problems.

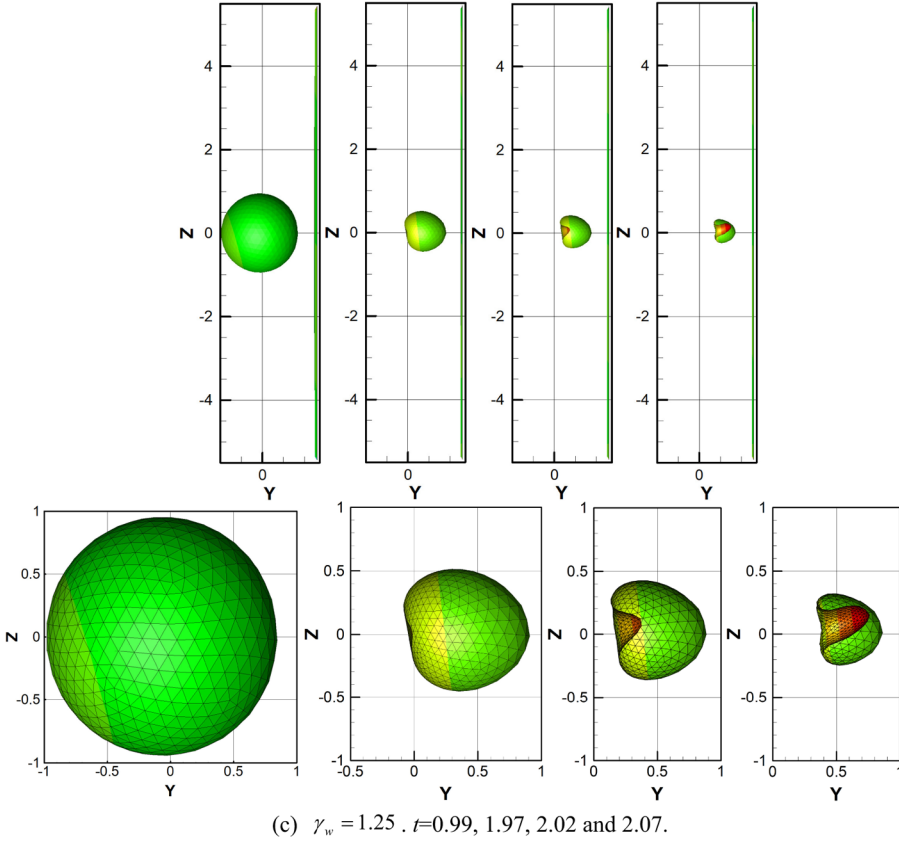


FIG. 7. (Continued.).

B. Fully nonlinear interaction between the bubble and the thin-walled plate

1. Basic phenomenon

In this section, we investigate the basic phenomenon of the dynamic interaction between the bubble and elastic-plastic thin-walled plate whose boundaries are rigidly fixed. The initial bubble radius $R_0 = 8.904$ mm, the maximum bubble radius $R_m = 0.112$ m, the initial distance from the bubble center to the plate center is 0.196 m, and the initial water depths of the bubble center and plate center are both 1 m. The thin-walled plate, whose side length is 1.2 m and thickness h is 20 mm, is positioned at the plane $y = 0.196$ m at the initial moment. The material parameters of the square plate are density $\rho_s = 7850$ kg/m³, elastic modulus $E = 203$ GPa, Poisson's ratio $\nu = 0.3$, yield stress $\sigma_0 = 235$ MPa, and tangent modulus $E_T = 400$ MPa. The ratio of the specific heat $\lambda = 1.25$. The vapor pressure $P_v = 0$. According to the above parameters, the reference values can be determined: $P_{\text{ref}} = 1.098 \times 10^5$ Pa, $V_{\text{ref}} = 10.48$ m/s, $T_{\text{ref}} = 1.07 \times 10^{-2}$ s, and $\phi_{\text{ref}} = 1.17$ m²/s. The dimensionless parameters are $\varepsilon = 588.76$ and $\gamma_w = 1.75$.

Figure 4 displays the nondimensional velocity potential contour with $\gamma_w = 1.75$ at typical times. Initially, the bubble expands spherically due to the inner high pressure. At $t = 0.96$, the bubble reaches the maximum volume. During the bubble collapse phase, the plate blocks the fluid motion directed toward the bubble, and the low pressure region appears near the right side of the bubble, which leads to the jet formation. Under the combined action of Bjerknes effects and the buoyancy, the high speed liquid jet moves to the top right. The bubble has dynamic behaviors similar to the results in [13]. The plate thickness is 20 mm in this case. Because of the high structural stiffness, it

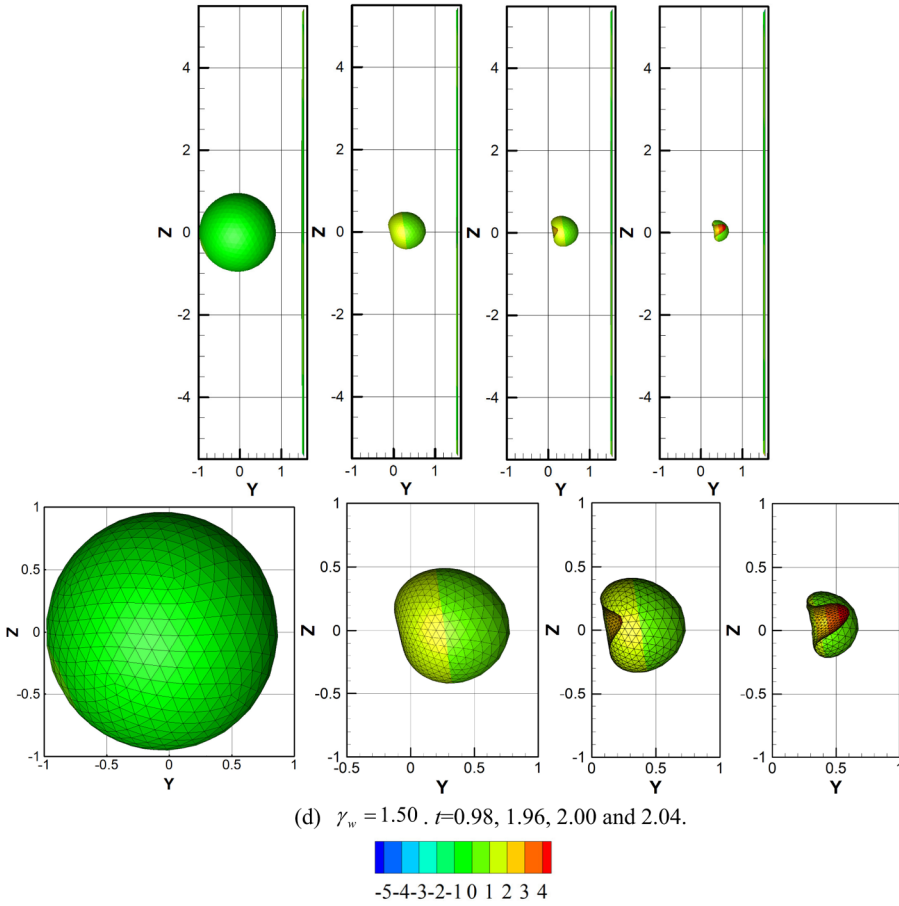


FIG. 7. (Continued.).

is hard to observe the plate deformation in the Fig. 4. The dimensionless plate displacement in the y direction is given in Fig. 5.

Figure 6 gives the time history of the bubble volume and plate center displacement. At the beginning of the bubble expansion phase, the fluid surrounding the bubble pushes the plate center to move away from the bubble. Afterward, the bubble kinetic energy begins to decrease and the velocity of the fluid between the bubble and plate slows down gradually due to the plate blocking. However, for the other side of the plate, the fluid disturbance caused by the bubble is relatively small, and the hydrodynamic pressure is nearly the ambient pressure. Therefore, the resultant force caused by the hydrodynamic pressure acting on the plate moves toward the bubble. The motion of the plate center is attracted by the bubble until the end of the expansion phase. When the bubble begins to collapse, the fluid disturbance caused by the bubble becomes strong gradually, with the bubble kinetic energy increasing. The resultant force acting on the plate directs away from the bubble. The plate center begins to move away from the bubble again. At the end of the bubble collapse phase, the high pressure region appears near the left side of the bubble, and the jet develops toward the plate; the plate center changes its motion direction again. It should be noted that we only focus on the bubble-structure interaction before the liquid jet penetrates the bubble surface in the present study. The highest deformations would appear after the jet hits the structure or after the toroidal bubble ring collapses.

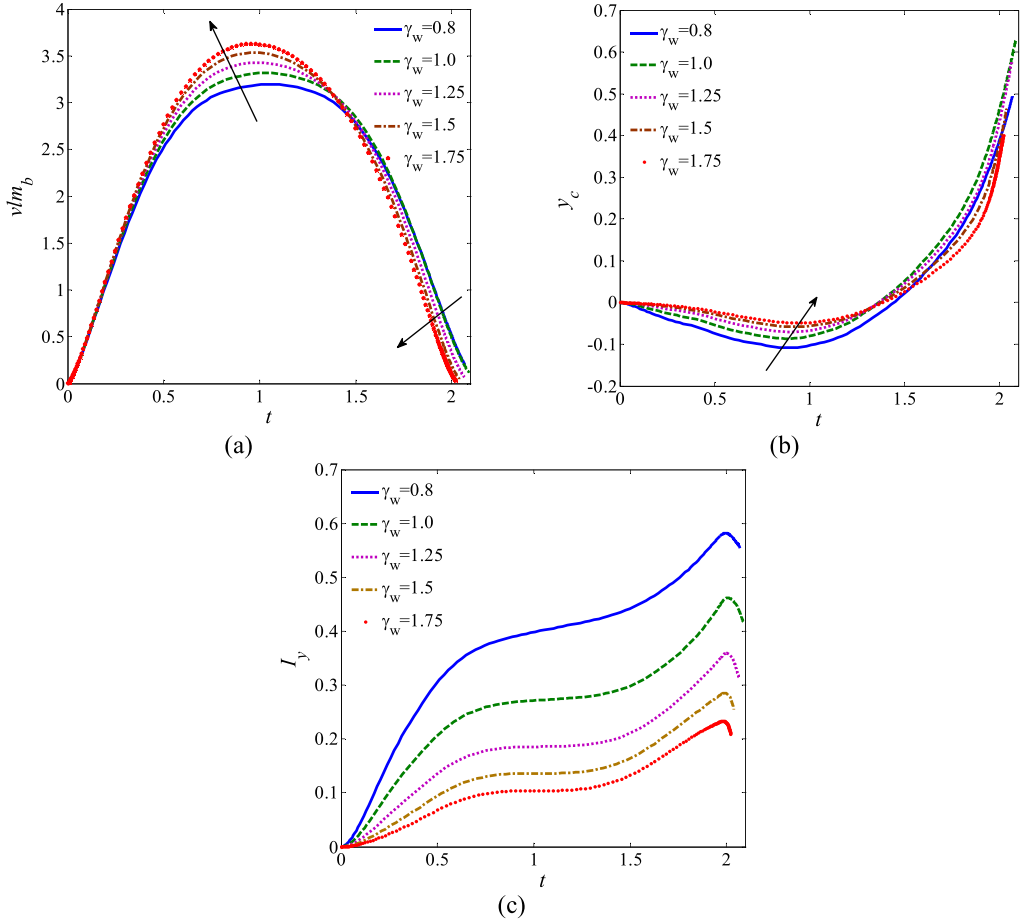


FIG. 8. Time evolution of bubble dynamics near a 20-mm-thick plate with different distance parameters for the case shown in Fig. 7. (a) Dimensionless bubble volume, (b) dimensionless bubble center, and (c) dimensionless Kelvin's impulse.

2. Effects of distance parameter

The distance parameter plays a significant role during the dynamic interaction between the bubble and rigid body [19]. In this section, the effects of the distance parameter on the bubble–deformable structure interaction are investigated. Five cases are simulated with $\gamma_w = 0.80, 1.00, 1.25, 1.50,$ and 1.75 , respectively. All the other parameters are kept the same as in Sec. III B 1.

Figure 7 shows the bubble dynamics with different γ_w . For the case $\gamma_w = 0.80$, the right part of the bubble becomes flattened by the plate at the end of the expansion phase. During the collapse phase, the bubble attaches to the plate. The jet will impinge on the structure boundary, which causes serious damage to the plate [2,24]. The bubble behaviors are similar in the other cases. The bubble remains almost spherical during the expansion phase. The bubble becomes kidney shaped and a liquid jet directs toward the plate at the end of the collapse phase. However, the distance parameter γ_w has an influence on the jet patterns. With the increase of the distance parameter, a thicker liquid jet develops earlier and points in the upper direction at the end of the collapse phase, as shown in Fig. 7. In this section, the coupling effects between the bubble and structure are relatively weak due to the structural stiffness. The overall bubble behaviors are similar to the bubble dynamics near a rigid wall.

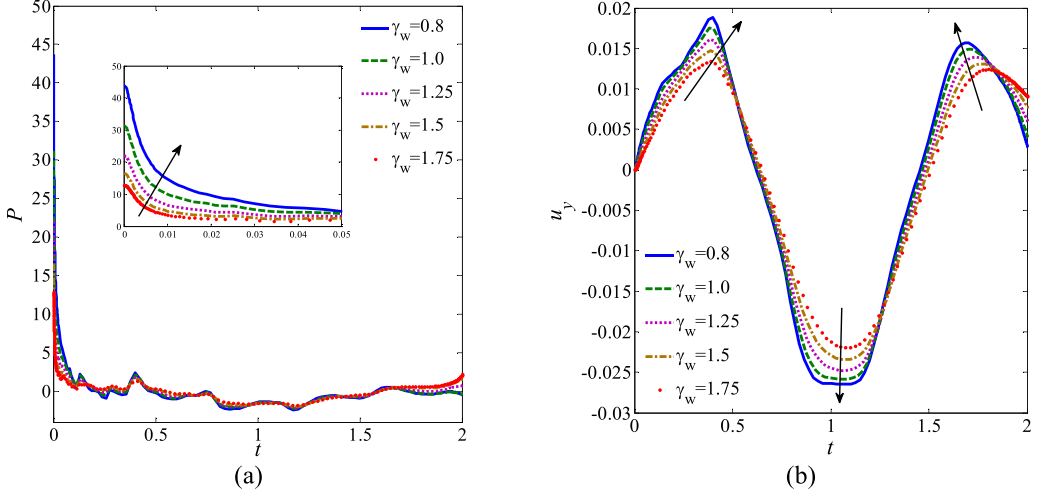


FIG. 9. Time evolution of the structural dynamics at the center of 20-mm-thick plate with different distance parameters for the case shown in Fig. 7. (a) Dimensionless hydrodynamic load, and (b) dimensionless displacement.

Figure 8 shows the history of the nondimensional bubble volume, bubble centroid y_c , and Kelvin impulse I_y with various standoff distances, where the arrow points to the increase of γ_w . The y component of the dimensionless Kelvin impulse $I_y = \int_{S_y} \phi n_y dS / [\phi_{\text{ref}} (L_{\text{ref}})^2]$ [11], where n_y denotes the y component of the unit normal vector \mathbf{n} . In this section the coupling effects between the bubble and plate are relatively weak. The properties of the plate tend to the rigid wall. With the distance parameter increasing, the maximum volume increases and the oscillation period slightly decreases, as depicted in Fig. 8(a). Figure 8(b) indicates that the bubble migrates away from the plate to a small extent during the expansion phase and then it obviously migrates to the plate. When the bubble volume is at its maximum, the migration velocity almost reaches the minimum and the bubble changes its motion direction. When the bubble is farther from the plate, the Bjerknes effect becomes weaker and the Kelvin impulse in the y direction gets smaller. Consequently, the bubble migrates slower with a larger distance parameter.

Figure 9(a) gives the histories of the hydrodynamic load at the plate center with different standoff distances, where the arrow points to the decrease of the distance parameter. The dimensionless hydrodynamic load in Fig. 9(a) $P = -\rho_l(\phi_t + \frac{1}{2}\nabla\phi \cdot \nabla\phi)|_{S_{S1}} + \rho_l(\phi_t + \frac{1}{2}\nabla\phi \cdot \nabla\phi)|_{S_{S2}}$, which denotes the difference between the hydrodynamic pressure on two sides of the plate. At the beginning, the hydrodynamic load at the plate center decreases rapidly, and decreases to a value of about 4 at the moment $t = 0.05$. Then it oscillates around the negative value during most of the pulsation period. Finally, the hydrodynamic load increases to a positive value. The standoff distance has a significant effect on the initial incident pressure peak. The initial pressure peak becomes larger at a smaller standoff distance.

The corresponding time evolution of the dimensionless displacement at the plate center is shown in Fig. 9(b). When the bubble is closer to the plate, the displacement amplitude becomes larger, but the standoff distance has little effect on the structural deformation frequency. For the case with $\gamma_w = 1.75$, the deformation of the plate center can reach the first amplitude. However, for the cases with $\gamma_w = 0.8$ and 1.0 , it can be found that the second displacement amplitude decreases obviously compared with the first amplitude. To analyze the mechanical behaviors of the plate, the von Mises stress ($\sigma_{\text{Mises}} = \sqrt{\hat{\sigma}_x^2 + \hat{\sigma}_y^2 - \hat{\sigma}_x\hat{\sigma}_y + 3\hat{\tau}_{xy}^2}$) distribution of the plate surface at $\gamma_w = 0.8$ is displayed in Fig. 10. As shown in this figure, the von Mises stress is smaller than the yield stress of the material during the whole simulation. According to the von Mises yield criterion, it can be seen that the plate

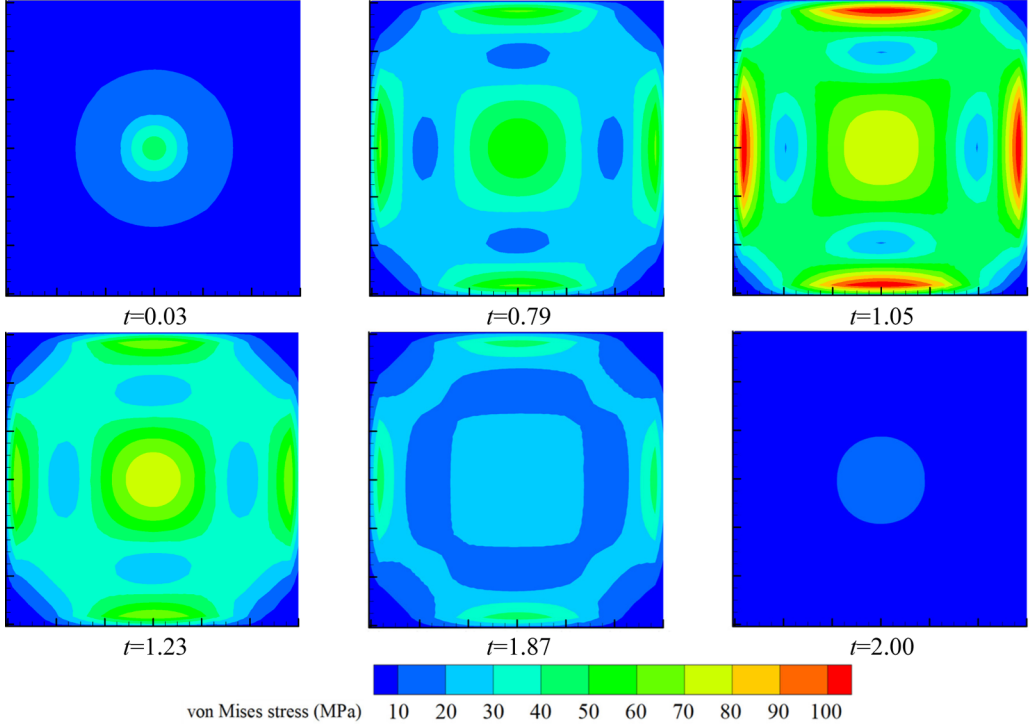


FIG. 10. Evolution of von Mises stress distribution of the plate at the location $\hat{z} = -9$ mm in thickness direction at $\gamma_w = 0.80$. All the parameters are the same as in Fig. 4.

does not undergo the plastic deformation in this case. Therefore, we infer that the attached bubble leads to the decrease of the second displacement amplitude. For the cases with the $\gamma_w = 0.8$ and 1.0, the bubble is very close to the plate surface after the moment around $t = 1$, as shown in Fig. 7. Due to the high pressure inside the bubble, the motion of the plate center is blocked and its second displacement amplitude decreases obviously compared with the first amplitude.

3. Effects of plate thickness

To investigate the strong coupled effects between the bubble and plate, the plate thickness h is set as 2 mm in this section. The distance parameter $\gamma_w = 0.80, 1.00, 1.25, 1.50, \text{ and } 1.75$. Other parameters are set the same as in Sec. III B 2. With the decrease of the plate thickness, the plate stiffness also decreases. The structure will undergo more violent deformation under the action of the same input bubble loading. The whole dynamic interaction process is accompanied by strong nonlinear coupled effects.

Figure 11 shows the dynamic interaction between the bubble and submerged thin plate with $\gamma_w = 0.8$ and 1.75. For the case with $\gamma_w = 0.8$, the bubble reaches the maximum volume and becomes an oblate spheroid at the moment $t = 0.65$. Afterward, under the influence of the boundary effects caused by the deformable plate, the bubble elongates in the axial direction, while it shrinks in the radial direction gradually. Finally, the radial width decreases to zero, and the whole bubble splits into two small bubbles. For the case with $\gamma_w = 1.75$, the bubble becomes a spheroid at its maximum volume. During the collapse phase, the high pressure region appears near the right side of the bubble. The liquid jet away from the plate develops rapidly.

Figure 12(a) displays the comparison of the dimensionless hydrodynamic load at the plate center with $\gamma_w = 1.75$ between different plate thicknesses, 2 and 20 mm. The initial hydrodynamic load is

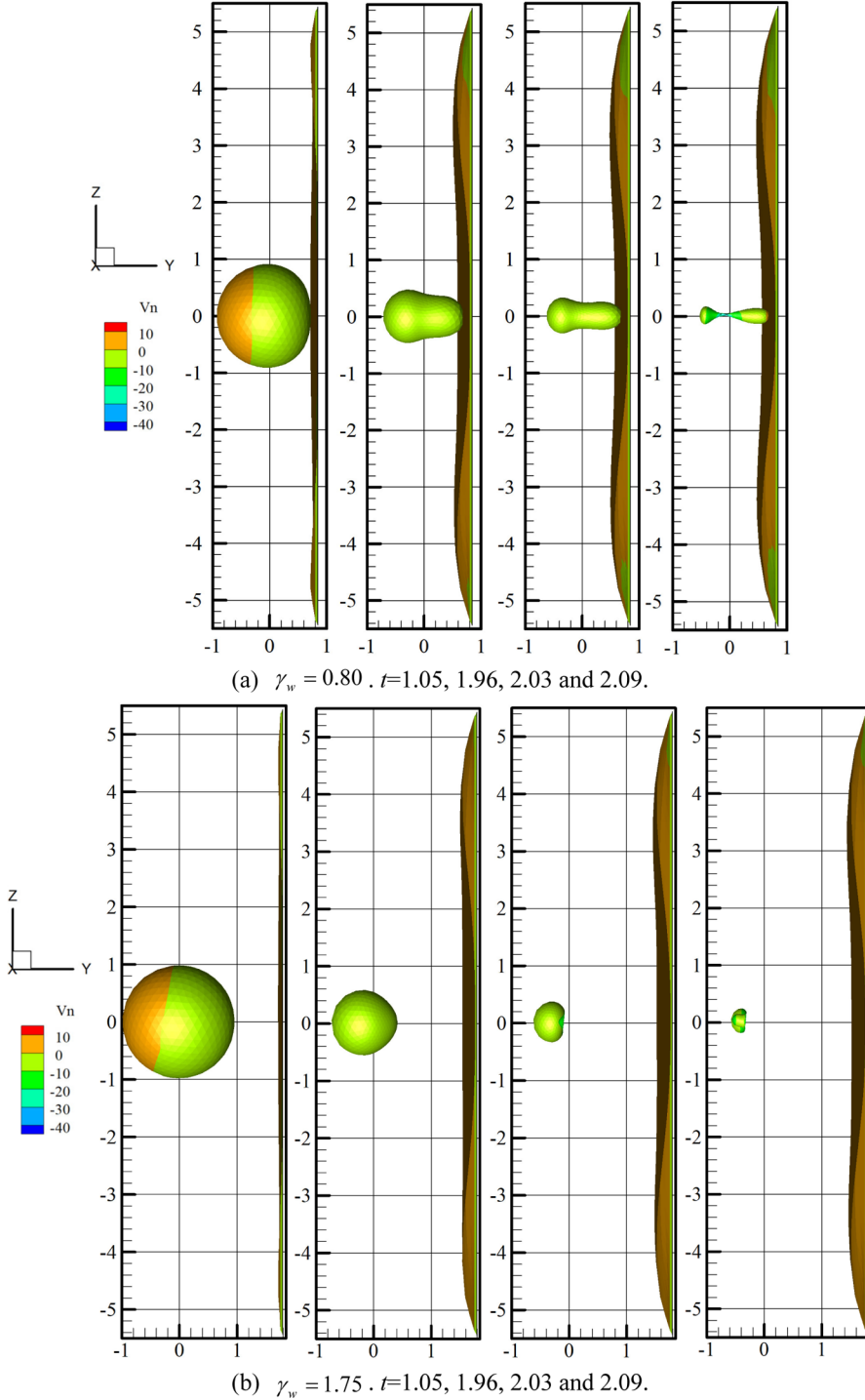


FIG. 11. Dimensionless normal velocity contour of the interaction between the bubble and the thin plate. (a) $\gamma_w = 0.80$; (b) $\gamma_w = 1.75$. The other parameters are $R_m = 0.112$ m, $R_0 = 8.904$ mm, $P_\infty = 1.098 \times 10^5$ Pa, $P_v = 0$, $\rho_s = 7850$ kg/m³, $E = 203$ GPa, $\nu = 0.3$, $\sigma_0 = 235$ MPa, $E_T = 400$ MPa, $h = 2$ mm, $\varepsilon = 588.76$, and $\lambda = 1.25$.

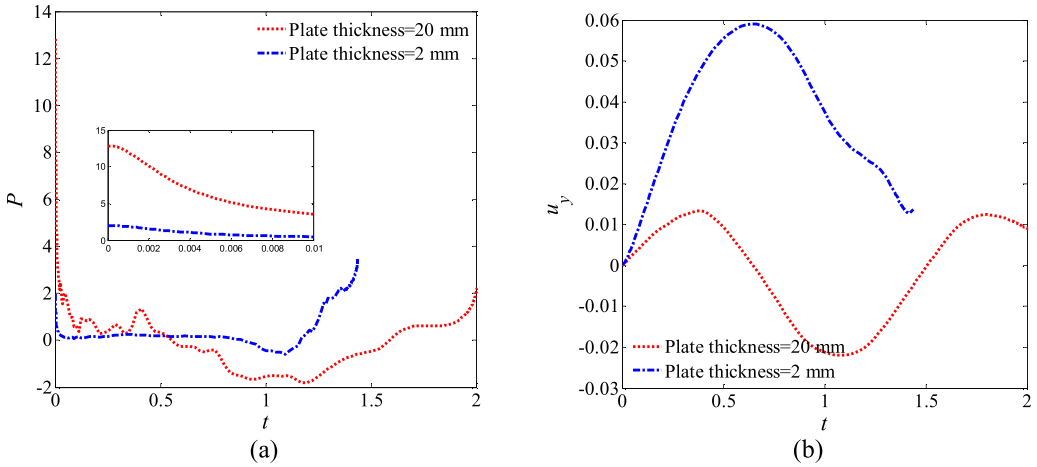


FIG. 12. Comparison of structural dynamics at the plate center between different plate thicknesses at $\gamma_w = 1.75$ for the case shown in Figs. 4 and 11(b). (a) Dimensionless hydrodynamic load, and (b) dimensionless displacement.

larger with the plate thickness of 20 mm, which can be explained as follows. The hydrodynamic load includes two parts, bubble pulsating pressure and added mass force due to the structural motion. Due to the same initial parameters of the bubble, the initial bubble pulsation pressures are the same for both cases. However, for the case with a thickness of 20 mm, the structural mass is larger than that of the case with a thickness of 2 mm, and the added mass force associated with structural acceleration becomes smaller. This leads to a larger hydrodynamic load at the initial moment. Figure 12(b) shows the time histories of the dimensionless displacement at the plate center with $\gamma_w = 1.75$. For the case with a thickness of 2 mm, the structural deformation is much larger due to the strong coupling effects. As shown in Fig. 11(a), the plate becomes convex shaped around the boundary.

Figure 13 displays the bubble jet patterns near an elastic-plastic plate with a thickness of 2 mm at various standoff distances. The results are obviously different from the bubble patterns near a plate with thickness of 20 mm in Fig. 7. For the plate with a thickness of 2 mm, the dynamic interaction between the bubble and plate becomes strongly nonlinear. Due to the influence of the elastic-plastic boundary, the bubble shows complex dynamic behaviors. For the case with $\gamma_w = 0.8$, the whole bubble will split into two small bubbles at the ending of the first pulsation period. For the other cases, a liquid jet forms in a direction away from the plate. The direction of the jet is opposite to the results with a plate thickness of 20 mm. With the standoff distance increasing, the jet width becomes larger. To analyze the cause of the repulsive jet, we display the dimensionless pressure contour of the fluid field around the bubble for the case with $\gamma_w = 1.50$ in Fig. 14. Compared with the 20-mm-thick plate, the structure stiffness of the 2-mm-thick plate decreases, and the coupled interaction between the bubble and plate becomes stronger. As shown in this figure, a high pressure zone appears between the bubble and the plate at the end of the bubble collapse phase, which makes the jet move away from the plate. An underwater explosion bubble near the aluminum plate boundary at $\gamma_w = 0.96$ and 0.63 in Hung and Hwangfu's experiment [44] has a similar behavior.

Figure 15 gives the time history of the dimensionless bubble center and bubble volume at different standoff distances, where the arrow points to the increase of standoff distance. For the case with $\gamma_w = 0.80$, the whole bubble eventually splits into two small bubbles. However, in other cases, the bubble develops a liquid jet, and the bubble center migrates away from the elastic-plastic plate. Therefore, the motion of the bubble center in the case with $\gamma_w = 0.80$ is different from that in cases with other distance parameters. In this study, the 2-mm-thick plate has a repulsion effect on the bubble, which is similar to the boundary properties of the free surface. With the standoff distance

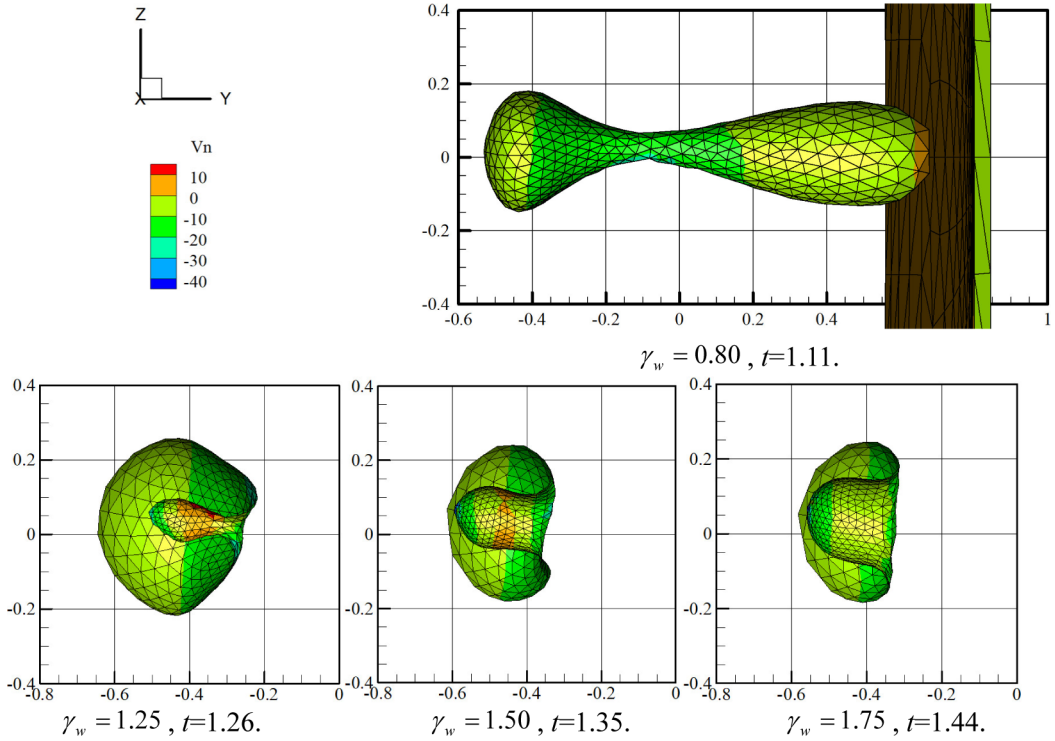


FIG. 13. Dimensionless normal velocity contour of bubble jet patterns near a 2-mm-thick plate for various distance parameters $\gamma_w = 0.80, 1.25, 1.50,$ and 1.75 with the remaining parameters being the same as in Fig. 11.

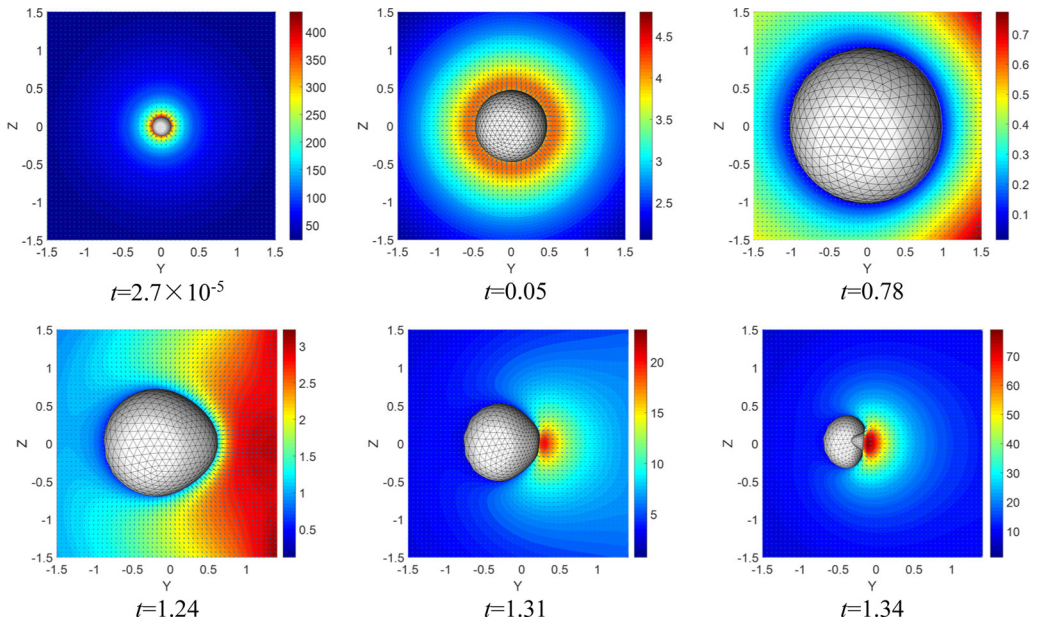


FIG. 14. Dimensionless pressure contour of the fluid field around the bubble for $\gamma_w = 1.50$ at typical dimensionless times. The other parameters are the same as in Fig. 11. The plate surface is not shown in this figure.

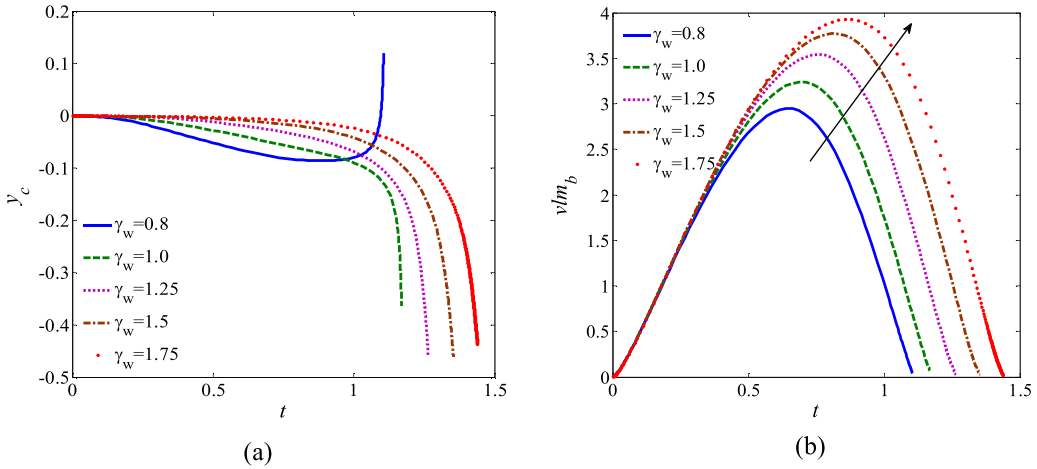


FIG. 15. Time evolution of bubble dynamics near a 2-mm-thick plate for various distance parameters $\gamma_w = 0.80, 1.0, 1.25, 1.50,$ and 1.75 with the remaining parameters being the same as in Fig. 11. (a) Dimensionless bubble center, and (b) dimensionless bubble volume.

increasing, the maximum volume of the bubble becomes larger, and the first pulsation period is lengthened, as shown in Fig. 15(b).

The time evolution of the dimensionless hydrodynamic pressure and displacement at the center of a 2-mm-thick plate is shown in Fig. 16. When the bubble is closer to the plate, the initial pressure amplitude and displacement amplitude become larger. Compared to the interaction phenomenon with a plate thickness of 20 mm in Fig. 9, the hydrodynamic pressure varies more violently, and the vibration period at the plate center becomes much longer when the plate thickness is 2 mm.

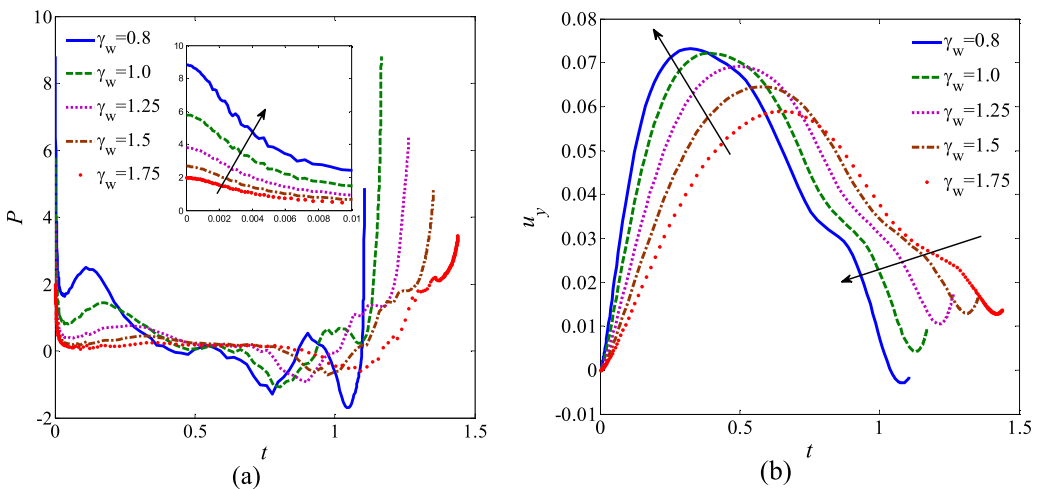


FIG. 16. Time evolution of the structural dynamics at the center of 2-mm-thick plate for various distance parameters $\gamma_w = 0.80, 1.0, 1.25, 1.50,$ and 1.75 with the remaining parameters being the same as in Fig. 11. (a) Dimensionless hydrodynamic load, and (b) dimensionless displacement.

IV. CONCLUSIONS

In this paper, we develop a fully coupled model to investigate the highly nonlinear dynamic behaviors of a bubble near an elastic-plastic thin-walled plate. The bubble dynamic behaviors are simulated by the BEM, and the transient dynamic responses of the elastic-plastic plate are resolved by the EFEM. The structural elastic-plastic responses are incorporated into the fluid governing equation, which can yield an extra BIE about ϕ_t jump across two sides of the thin-walled plate and ϕ_{in} . The derived relationship is added to the original BIE about ϕ_t , so that the bubble loading acting on the plate surface can be directly calculated. The present model can accurately describe the structural motion coupling with the flow field on two sides of the thin-walled plate.

In this study, an elastic-plastic plate with a thickness of 20 mm has an attractive effect on the nearby bubble. At the end of the bubble collapse phase, the bubble forms a liquid jet moving to the plate. With the standoff distance increasing, the maximal bubble volume increases and the oscillation period slightly decreases. When the bubble is closer to the plate, the displacement amplitude becomes larger. But the standoff distance has little effect on the structural vibration frequency. For the cases with $\gamma_w = 0.8$ and $\gamma_w = 1.0$, the bubble is very close to the plate surface after the moment around $t = 1$. Due to the high pressure inside the bubble, the motion of the plate center is blocked and its second displacement amplitude decreases obviously compared with the first amplitude.

When the bubble interacts with an elastic-plastic plate whose thickness is 2 mm, the bubble appears in different jet patterns at various standoff distances. For the cases with $\gamma_w = 0.8$, the whole bubble splits into small bubbles at the end of the contraction phase. In the other cases, the plate has a repulsive effect on the bubble. The bubble develops a jet moving away from the plate. With the standoff distance increasing, the jet width becomes larger, and the first pulsation period is lengthened. Compared to the interaction phenomenon with a plate thickness of 20 mm, the hydrodynamic pressure varies more violently, and the vibration period at the plate center becomes much longer when the plate thickness is 2 mm.

ACKNOWLEDGMENTS

The work has been supported by the National Natural Science Foundation of China (Grant No. 52001010), the China Postdoctoral Science Foundation (Grant No. 2020M670046), and the Science Challenge Project (Grant No. TZ2018002).

-
- [1] J. R. Blake and D. C. Gibson, Cavitation bubbles near boundaries, *Annu. Rev. Fluid Mech.* **19**, 99 (1987).
 - [2] Q. X. Wang, Multi-oscillations of a bubble in a compressible liquid near a rigid boundary, *J. Fluid Mech.* **745**, 509 (2014).
 - [3] Y. Liu, K. Sugiyama, S. Takagi, and Y. Matsumoto, Surface instability of an encapsulated bubble induced by an ultrasonic pressure wave, *J. Fluid Mech.* **691**, 315 (2012).
 - [4] J. R. Lindner, Microbubbles in medical imaging: Current applications and future directions, *Nat. Rev. Drug Discovery* **3**, 527 (2004).
 - [5] E. C. Unger, E. Hersh, M. Vannan, T. O. Matsunaga, and T. McCreery, Local drug and gene delivery through microbubbles, *Prog. Cardiovasc. Dis.* **44**, 45 (2001).
 - [6] K. Manmi, W. B. Wu, N. Vyas, W. R. Smith, Q. X. Wang, and A. D. Walmsley, Numerical investigation of cavitation generated by an ultrasonic dental scaler tip vibrating in a compressible liquid, *Ultrason. Sonochem.* **63**, 104963 (2020).
 - [7] G. L. Chahine, K. M. Kalumuck, and C. T. Hsiao, Simulation of surface piercing body coupled response to underwater bubble dynamics utilizing 3DYNAFS, a three-dimensional BEM code, *Comput. Mech.* **32**, 319 (2003).

- [8] Q. X. Wang, Local energy of a bubble system and its loss due to acoustic radiation, *J. Fluid Mech.* **797**, 201 (2016).
- [9] W. B. Wu, Y. L. Liu, and A. M. Zhang, Numerical investigation of 3D bubble growth and detachment, *Ocean Eng.* **138**, 86 (2017).
- [10] X. Y. Kan, A. M. Zhang, J. L. Yan, W. B. Wu, and Y. L. Liu, Numerical investigation of ice breaking by a high pressure bubble based on a coupled BEM-PD model, *J. Fluid Struct.* **96**, 103016 (2020).
- [11] J. R. Blake, B. B. Taib, and G. Doherty, Transient cavities near boundaries. Part 1. Rigid boundary, *J. Fluid Mech.* **170**, 479 (1986).
- [12] J. R. Blake, B. B. Taib, and G. Doherty, Transient cavities near boundaries. Part 2. Free surface, *J. Fluid Mech.* **181**, 197 (1987).
- [13] Q. X. Wang, The evolution of a gas bubble near an inclined wall, *Theor. Comput. Fluid Dyn.* **12**, 29 (1998).
- [14] A. Zhang and Y. Liu, Improved three-dimensional bubble dynamics model based on boundary element method, *J. Comput. Phys.* **294**, 208 (2015).
- [15] E. Klaseboer, K. C. Hung, C. Wang, C. W. Wang, B. C. Khoo, P. Boyce, S. Debono, and H. Charlier, Experimental and numerical investigation of the dynamics of an underwater explosion bubble near a resilient/rigid structure, *J. Fluid Mech.* **537**, 387 (2005).
- [16] C. T. Hsiao, A. Jayaprakash, and A. Kapahi, Modelling of material pitting from cavitation bubble collapse, *J. Fluid Mech.* **755**, 142 (2014).
- [17] C. T. Hsiao and G. L. Chahine, Dynamic response of a composite propeller blade subjected to shock and bubble pressure loading, *J. Fluids Struct.* **54**, 760 (2015).
- [18] Z. Zong, J. X. Wang, and L. Zhou, Fully nonlinear 3D interaction of bubble dynamics and a submerged or floating structure, *Appl. Ocean Res.* **53**, 236 (2015).
- [19] S. Li, A. M. Zhang, R. Han, and Q. W. Ma, 3D full coupling model for strong interaction between a pulsating bubble and a movable sphere, *J. Comput. Phys.* **392**, 713 (2019).
- [20] K. Tanizawa, A nonlinear simulation method of 3-D body motions in waves (1st report), *J. Soc. Nav. Archit. Jpn.* **178**, 179 (1995).
- [21] Y. L. Liu, A. M. Zhang, Z. L. Tian, and S. P. Wang, Numerical investigation on global responses of surface ship subjected to underwater explosion in waves, *Ocean Eng.* **161**, 277 (2018).
- [22] W. Koo and M.-H. Kim, Freely floating-body simulation by a 2D fully nonlinear numerical wave tank, *Ocean Eng.* **31**, 2011 (2004).
- [23] E. Guerber, Numerical modelling of nonlinear interactions of waves with submerged structures: Applied to the simulation of wave energy converters, Ph.D. thesis, Universite Paris-Est, 2011.
- [24] A. M. Zhang, W. B. Wu, Y. L. Liu, and Q. X. Wang, Nonlinear interaction between underwater explosion bubble and structure based on fully coupled model, *Phys. Fluids* **29**, 082111 (2017).
- [25] P. Cui, A. M. Zhang, and S. P. Wang, Small-charge underwater explosion bubble experiments under various boundary conditions, *Phys. Fluids* **28**, 117103 (2016).
- [26] S. Zhu, F. H. Cocks, G. M. Preminger, and P. Zhong, The role of stress waves and cavitation in stone comminution in shock wave lithotripsy, *Ultrasound Med. Biol.* **28**, 661 (2002).
- [27] Y. L. Zhang, K. S. Yeo, B. C. Khoo, and C. Wang, 3D jet impact and toroidal bubbles, *J. Comput. Phys.* **166**, 336 (2001).
- [28] C. Wang and B. Khoo, An indirect boundary element method for three-dimensional explosion bubbles, *J. Comput. Phys.* **194**, 451 (2004).
- [29] J. Best, The formation of toroidal bubbles upon the collapse of transient cavities, *J. Fluid Mech.* **251**, 79 (1993).
- [30] M. Longuet-Higgins and E. D. Cokelet, The deformation of steep surface waves on water: I. A numerical method of computation, *Proc. R. Soc. London, Ser. A* **350**, 1 (1976).
- [31] J. P. Best and A. Kucera, A numerical investigation of non-spherical rebounding bubbles, *J. Fluid Mech.* **245**, 137 (1992).
- [32] T. Belytschko, H. Stolarski, and N. Carpenter, A C^0 triangular plate element with one-point quadrature, *Int. J. Numer. Methods Eng.* **20**, 787 (1984).

- [33] T. J. R. Hughes, *The Finite Element Method: Linear Static and Dynamic Finite Element Analysis* (Dover, Mineola, NY, 2000).
- [34] O. C. Zienkiewicz, R. L. Taylor, and J. Z. Zhu, *The Finite Element Method: Its Basis and Fundamentals*, 7th ed. (Butterworth-Heinemann, Oxford, 2013).
- [35] T. Belytschko, A survey of numerical methods and computer programs for dynamic structural analysis, *Nucl. Eng. Des.* **37**, 23 (1976).
- [36] D. P. Flanagan and T. Belytschko, Simultaneous relaxation in structural dynamics, *J. Eng. Mech. Div.* **107**, 1039 (1981).
- [37] S. R. Wu and L. Gu, *Introduction to the Explicit Finite Element Method for Nonlinear Transient Dynamics* (John Wiley & Sons, Inc., Hoboken, NJ, 2012).
- [38] *LS-DYNA Theoretical Manual* (Livermore Software Technology Corporation (LSTC), Livermore, CA, 1998).
- [39] Z. L. Tian, Y.-L. Liu, A.-M. Zhang, and L. Tao, Energy dissipation of pulsating bubbles in compressible fluids using the Eulerian finite-element method, *Ocean Eng.* **196**, 106714 (2020).
- [40] A. H. Aghdam, S. W. Ohl, B. C. Khoo, M. T. Shervani-Tabar, and M. R. H. Nobari, Effect of the viscosity on the behavior of a single bubble near a membrane, *Int. J. Multiphase Flow* **47**, 17 (2012).
- [41] S. Buogo and G. B. Cannelli, Implosion of an underwater spark-generated bubble and acoustic energy evaluation using the Rayleigh model, *J. Acoust. Soc. Am.* **111**, 2594 (2002).
- [42] C. K. Turangan, G. P. Ong, E. Klaseboer, and B. C. Khoo, Experimental and numerical study of transient bubble–elastic membrane interaction, *J. Appl. Phys.* **100**, 054910 (2006).
- [43] M. T. Shervani-Tabar, A. Hajizadeh Aghdam, B. C. Khoo, V. Farhangmehr, and B. Farzaneh, Numerical analysis of a cavitation bubble in the vicinity of an elastic membrane, *Fluid Dyn. Res.* **45**, 055503 (2013).
- [44] C. F. Hung and J. J. Hwangfu, Experimental study of the behavior of mini-charge underwater explosion bubbles near different boundaries, *J. Fluid Mech.* **651**, 55 (2010).